Article

Millimetre-scale bioresorbable optoelectronic systems for electrotherapy

https://doi.org/10.1038/s41586-025-08726-4

Received: 14 February 2024

Accepted: 31 January 2025

Published online: 2 April 2025

Check for updates

Yamin Zhang[1,2,3,21]✉, Eric Rytkin[4,21], Liangsong Zeng[2,5,21], Jong Uk Kim[1,2,21], Lichao Tang[3,21], Haohui Zhang[6,21], Aleksei Mikhailov[7], Kaiyu Zhao[2,8], Yue Wang[2,4], Li Ding[2,9], Xinyue Lu[2], Anastasia Lantsova[4], Elena Aprea[2,10], Gengming Jiang[2], Shupeng Li[5], Seung Gi Seo[1,2], Tong Wang[11], Jin Wang[2], Jiayang Liu[8], Jianyu Gu[1,2], Fei Liu[2,8], Keith Bailey[12], Yat Fung Larry Li[8], Amy Burrell[13], Anna Pfenniger[7], Andrey Ardashev[7], Tianyu Yang[1,2], Naijia Liu[1,2], Zengyao Lv[6], Nathan S. Purwanto[8], Yue Ying[14], Yinsheng Lu[2,8], Claire Hoepfner[2], Altynai Melisova[4], Jiarui Gong[15], Jinheon Jeong[16], Junhwan Choi[17], Alex Hou[2,4], Rachel Nolander[2,4], Wubin Bai[18], Sung Hun Jin[16], Zhenqiang Ma[15], John M. Torkelson[8,11], Yonggang Huang[5]✉, Wei Ouyang[1,2,19]✉, Rishi K. Arora[7,20]✉, Igor R. Efimov[2,4,7]✉ & John A. Rogers[1,2,4,5,8]✉

Temporary pacemakers are essential for the care of patients with short-lived bradycardia in post-operative and other settings[1–4]. Conventional devices require invasive open-heart surgery or less invasive endovascular surgery, both of which are challenging for paediatric and adult patients[5–8]. Other complications[9–11] include risks of infections, lacerations and perforations of the myocardium, and of displacements of external power supplies and control systems. Here we introduce a millimetre-scale bioresorbable optoelectronic system with an onboard power supply and a wireless, optical control mechanism with generalized capabilities in electrotherapy and specific application opportunities in temporary cardiac pacing. The extremely small sizes of these devices enable minimally invasive implantation, including percutaneous injection and endovascular delivery. Experimental studies demonstrate effective pacing in mouse, rat, porcine, canine and human cardiac models at both single-site and multi-site locations. Pairing with a skin-interfaced wireless device allows autonomous, closed-loop operation upon detection of arrhythmias. Further work illustrates opportunities in combining these miniaturized devices with other medical implants, with an example of arrays of pacemakers for individual or collective use on the frames of transcatheter aortic valve replacement systems, to provide unique solutions that address risks for atrioventricular block following surgeries. This base technology can be readily adapted for a broad range of additional applications in electrotherapy, such as nerve and bone regeneration, wound therapy and pain management.

Temporary pacemakers are essential life-saving technologies for patients who suffer from short-lived bradycardia, typically on the order of days or weeks[1–4]. Applications include post-operative care after cardiac surgery, a heart attack or a medication overdose. Most adult patients and paediatric patients receive a temporary pacemaker after cardiac surgery. Conventional temporary pacing requires epicardial or transvenous placements of pacing leads, which necessitates invasive open-heart or endovascular surgeries. The former can lead to difficult post-surgery recovery processes, extended hospitalization times and significant surgical scars. Endovascular surgeries are challenging for adult patients with contraindications to transvenous pacemakers and for paediatric patients with small body sizes and rapid patterns of growth[5–8]. Other complications[9–11] include risks of infections with the pacing leads and their percutaneous access points, of lacerations and perforations of the myocardium owing to removal or replacement of these leads, and of displacements of external power

[1]Center for Bio-Integrated Electronics, Northwestern University, Evanston, IL, USA. [2]Querrey Simpson Institute for Bioelectronics, Northwestern University, Evanston, IL, USA. [3]Department of Chemical and Biomolecular Engineering, National University of Singapore, Singapore, Singapore. [4]Department of Biomedical Engineering, Northwestern University, Evanston, IL, USA. [5]Department of Mechanical Engineering, Northwestern University, Evanston, IL, USA. [6]Department of Civil and Environmental Engineering, Northwestern University, Evanston, IL, USA. [7]Feinberg Cardiovascular and Renal Research Institute, Northwestern University Feinberg School of Medicine, Chicago, IL, USA. [8]Department of Materials Science and Engineering, Northwestern University, Evanston, IL, USA. [9]Department of Cardiovascular Surgery, Union Hospital, Tongji Medical College, Huazhong University of Science and Technology, Wuhan, China. [10]The BioRobotics Institute and Department of Excellence in Robotics and AI, Scuola Superiore Sant'Anna, Pisa, Italy. [11]Department of Chemical and Biological Engineering, Northwestern University, Evanston, IL, USA. [12]Alnylam Pharmaceuticals Inc, Cambridge, MA, USA. [13]Center for Comparative Medicine, Northwestern University Feinberg School of Medicine, Chicago, IL, USA. [14]Department of Electrical and Computer Engineering, Northwestern University, Evanston, IL, USA. [15]Department of Electrical and Computer Engineering, University of Wisconsin-Madison, Madison, WI, USA. [16]Department of Electronic Engineering, Incheon National University, Incheon, Republic of Korea. [17]Department of Chemical Engineering, Dankook University, Yongin, Republic of Korea. [18]Department of Applied Physical Sciences, University of North Carolina at Chapel Hill, Chapel Hill, NC, USA. [19]Thayer School of Engineering, Dartmouth College, Hanover, NH, USA. [20]The University of Chicago Medicine, University of Chicago, Chicago, IL, USA. [21]These authors contributed equally: Yamin Zhang, Eric Rytkin, Liangsong Zeng, Jong Uk Kim, Lichao Tang, Haohui Zhang. ✉e-mail: ymzhang@nus.edu.sg; y-huang@northwestern.edu; wei.ouyang@dartmouth.edu; rishi.arora@bsd.uchicago.edu; igor.efimov@northwestern.edu; jrogers@northwestern.edu

supplies and control systems. These circumstances create a pressing need for alternative technologies and surgical procedures. Recent studies on bioresorbable devices and on materials-oriented strategies address certain challenges, but with important limitations owing to their physical sizes, surgical demands, patient burdens and operating mechanisms[1,6,12–17].

As a superior solution to these clinical needs, we introduce a millimetre-scale, bioresorbable optoelectronic system with an onboard power supply and a wireless, optical control mechanism capable of addressing a broad range of applications in electrotherapy, with a focus here on temporary cardiac pacing. Unlike conventional pacing mechanisms that require pacing leads and separate power supplies, this technology directly utilizes battery electrodes as pacing electrodes. The extremely small size (1.8 mm × 3.5 mm × 1 mm) of this self-powered and leadless technology, more than 2.5 times smaller than any previously reported device[6,12–16] and more than 23 times smaller than any bioresorbable alternative[1,17] (Extended Data Fig. 1), minimizes the device load on and risks to the patient. The result allows for application even with neonates, and enables implantation using minimally invasive surgical techniques. Demonstrated options include percutaneous injection and endovascular delivery with additional opportunities for combined use with other medical procedures and devices, including transcatheter aortic valve replacement (TAVR) procedures. Additional distinguishing features include the ability to: (1) pair with a soft, skin-interfaced, wireless unit that continuously captures electrocardiograms (ECGs), performs data analytics, and optically controls the pacemaker as the basis for autonomous, closed-loop operation upon detection of cardiac arrhythmias; (2) pace in a multi-site manner with a wavelength-division multiplexing (WDM) technique for time-synchronized dual-chamber and biventricular pacing, including multi-site resynchronization therapy; (3) operate collections of devices directly integrated onto implantable frameworks, including TAVR stents; and (4) allow for medical imaging owing to compatibility with magnetic resonance imaging and computed tomography.

Materials, designs and mechanisms

Figure 1a shows schematic illustrations of the key design aspects. The pacemaker shown here has a weight of approximately 13.8 mg and dimensions of 1.8 mm × 3.5 mm and a thickness of 1 mm, comparable to the size of a grain of rice (Fig. 1b,d). The device exploits a self-powered mechanism, where the battery electrodes are the pacing electrodes. Specifically, an active, bioresorbable magnesium (Mg) alloy AZ31 ($Mg_{96}Al_3Zn_1$) foil or a zinc (Zn) composite (1.6 mm × 1.6 mm) serves as the anode, and a more electropositive bioresorbable molybdenum trioxide (MoO_3) composite (1.6 mm × 1.6 mm) serves as the cathode[18–20]. The cardiac tissue and associated biofluids act as the electrolyte to form a galvanic cell/battery (Mg–MoO_3 or Zn–MoO_3). As a demonstration, the pacemaker utilizes the Mg–MoO_3 pair if not otherwise specified. The two electrodes electrically interconnect through a silicon (Si) bipolar junction phototransistor (Supplementary Figs. 1 and 2), designed to respond at tissue-penetrating wavelengths in the near-infrared (NIR) range. This component provides an optical mechanism to control the operation of the device with an external light source. In particular, the anode and cathode connect to the emitter and the collector terminals of the phototransistor, respectively, using a biodegradable conductive paste (Candelilla wax/tungsten (W) powder)[21]. A bioresorbable formulation of polyanhydride[22] or wax[21] encapsulates the entire structure, leaving regions of the electrodes exposed to the interface with the cardiac tissue. These unusual materials, components, and operating mechanisms serve as the basis for the pacing technology.

The extremely small sizes of these devices allow for their delivery by minimally invasive percutaneous injection, as illustrated in Fig. 1c. Specifically, the pacemakers reported here can fit into small-diameter (<3 mm) introducers (Fig. 1d; 8 or 9 Fr (French gauge)), for injection directly into the superficial subepicardial layer of the myocardium through skin incisions with widths less than 3 mm. Pairing a pacemaker with a soft, skin-interfaced wireless device that supports the collection of electrocardiogram (ECG) data, analysis of these data and programmed light emission in the NIR range allows autonomous, closed-loop cardiac electrotherapy upon detection of arrhythmias (Fig. 1e). Here, pacing follows from illumination through the skin and underlying tissue, as described in the following. Figure 1f and Supplementary Fig. 3 show the mechanism. In the absence of illumination, the pacemaker is inactive because the high resistance of the phototransistor (about $10^6\ \Omega$) prevents flow of current in the galvanic cell. Upon illumination, the resistance of the phototransistor decreases by several orders of magnitude to about $10^2\ \Omega$, thereby closing the circuit and discharging the battery formed by the pacing electrodes and the adjacent cardiac tissue (Extended Data Fig. 2). During the discharge (Supplementary Figs. 3 and 4), the Mg anode undergoes an oxidation reaction ($Mg - 2e^- \rightarrow Mg^{2+}$), and the cathode undergoes a reduction reaction ($MoO_3 + ne^- \rightarrow MoO_3^{n-}$). Finite element analysis (Fig. 1g) reveals the distribution of the current density in the tissue for a transient pacing current of 0.5 mA cm^{-2}. The fast responses of the phototransistor and the overall optoelectronic circuit allow for precise, dynamic control over the current delivered to the heart. Compatibility of the devices with magnetic resonance imaging and computed tomography (Supplementary Figs. 5–7 and Supplementary Note 1) provides additional benefits for patients who require routine medical imaging.

All materials, including the electrodes, the phototransistor, the conductive pastes[21] and the packaging structure[22], are bioresorbable except for about 1.6 wt% of biocompatible carbon black as conductive additives for the cathodes. Replacing the carbon black with molybdenum (Mo) metal powder enables full bioresorption but results in a slightly larger size for comparable performance (Supplementary Fig. 8). Complete or partial bioresorption eliminates the need for surgical extraction after a period of operation (Fig. 1h). Figure 1i shows the results of accelerated tests of bioresorption that involve submerging a pacemaker (anode, 250-μm-thick Mg alloy; cathode, 500-μm-thick MoO_3 composite on a 5-μm-thick Mo, approximately 10-μm-thick phototransistor, and 100-μm-thick polyanhydride (1:1:2.5) encapsulation) in phosphate-buffered saline (pH 7.4) at 95 °C followed by transfer to a pH 10 buffer solution to complete the process. The products of degradation are $Mg(OH)_2$, H_2MoO_4, $Si(OH)_4$ and carboxylic acids, respectively; each is water soluble and capable of excretion by the kidneys[22,23–25]. In vitro cytocompatibility and in vivo biocompatibility studies reveal no adverse effects (Supplementary Figs. 9 and 10, and Supplementary Note 2). These results and additional analysis (Supplementary Note 3 and Supplementary Table 1) suggest a timescale for complete bioresorption of approximately 1.2–2.5 years[26,27]. Appropriate choices of materials and device designs can enable reductions in the bioresorption timescales by about two times[28,29] (Supplementary Note 3).

Characteristics and ex vivo pacing

Passing pulsed NIR light from a source located on or near the surface of the skin activates the delivery of electrical impulses to the heart, with rise and fall times aligned to those of the pulses to within less than 25 μs (Fig. 2a), far beyond the requirements for cardiac pacing. As discussed earlier, the pacing electrodes and the cardiac tissue form a battery that provides power for the pacing process. The phototransistor acts only as a passive switch, capable of activation at low intensities. Electrically connecting pacing electrodes embedded in soft chicken muscle tissue with a phototransistor and an ammeter in series allows measurement of the output of a pacemaker under different pulsed light intensities (Fig. 2b). The values are 0.02 mA, 0.22 mA, 0.45 mA and 0.64 mA at intensities of 0.001 mW mm^{-2}, 0.01 mW mm^{-2}, 0.02 mW mm^{-2} and 0.05 mW mm^{-2}, respectively. Supplementary Note 4 and Supplementary Figs. 11 and 12 show comprehensive

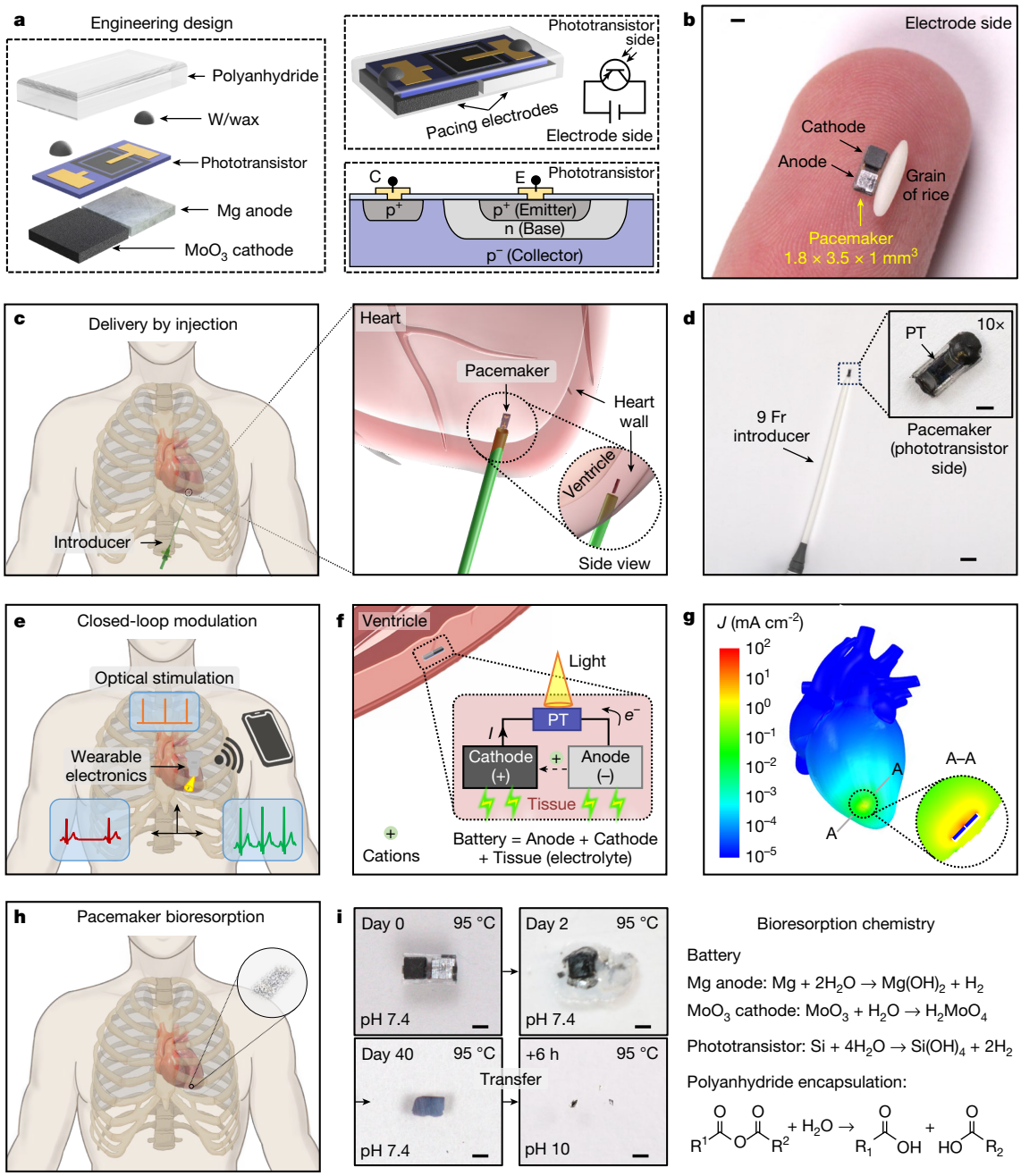

Fig. 1 | Design of injectable, self-powered, bioresorbable cardiac pacemakers with wireless, optoelectronic control. a, Engineering design. Left: exploded view illustration. Top right: schematic illustration and the equivalent circuit. Bottom right: structure of the phototransistor. E, emitter; C, collector. **b**,**d**, Photographs of pacemakers from the electrode side (**b**) and from the phototransistor (PT) side (**d**). **c**, Schematic illustrations of implantation via catheter injection. **e**, Pairing with a skin-interfaced optoelectronic device allows autonomous, closed-loop cardiac electrotherapy. **f**, Schematic diagram of the light-controlled, self-powered pacing mechanism. Illuminating the phototransistor decreases its electrical resistance and thus discharges the electrochemical cell formed by the anode and cathode with surrounding tissue and biofluids as the electrolyte. *I*, electric current. **g**, Finite element analysis results showing the current density (*J*) distribution in the heart for operation of a pacemaker at a current of 0.5 mA under light illumination. **h**,**i**, Schematic illustration (**h**), and photographs and chemistries (**i**) of bioresorption of a pacemaker. Photographs show the accelerated tests of bioresorption and indicate bioresorbability of the pacemaker. Scale bars, 1 mm (**b**, inset in **d**, and **i**) and 1 cm (**d**). Illustration of the heart in **c**, **e** and **h** was created with TurboSquid. Illustrations of the Wi-Fi signal and smartphone in **e** and the ventricle in **f** were created with BioRender (https://biorender.com).

technical specifications. Electrochemical impedance spectroscopy of the pacemaker (Supplementary Fig. 13) and measurements of phototransistor resistance (Extended Data Fig. 2) indicate that the battery resistance dominates the output current at NIR light intensities above approximately 0.05 mW mm^{-2}, which explains the observed saturation behaviour. The low sensitivity to intensity in this regime ensures stable operation even with fluctuations that can result from body motions.

Ex vivo pacing experiments on Langendorff-perfused porcine and human hearts demonstrate the functionality of pacemakers inserted into the superficial subepicardial layers of the myocardium. The illumination intensity, frequency and duty cycle control the current, rate and pulse width of the pacing process, respectively. Measurements of the strength–duration curve for pacing the porcine heart (Fig. 2c,d and Supplementary Fig. 14) indicate that the rheobase and chronaxie

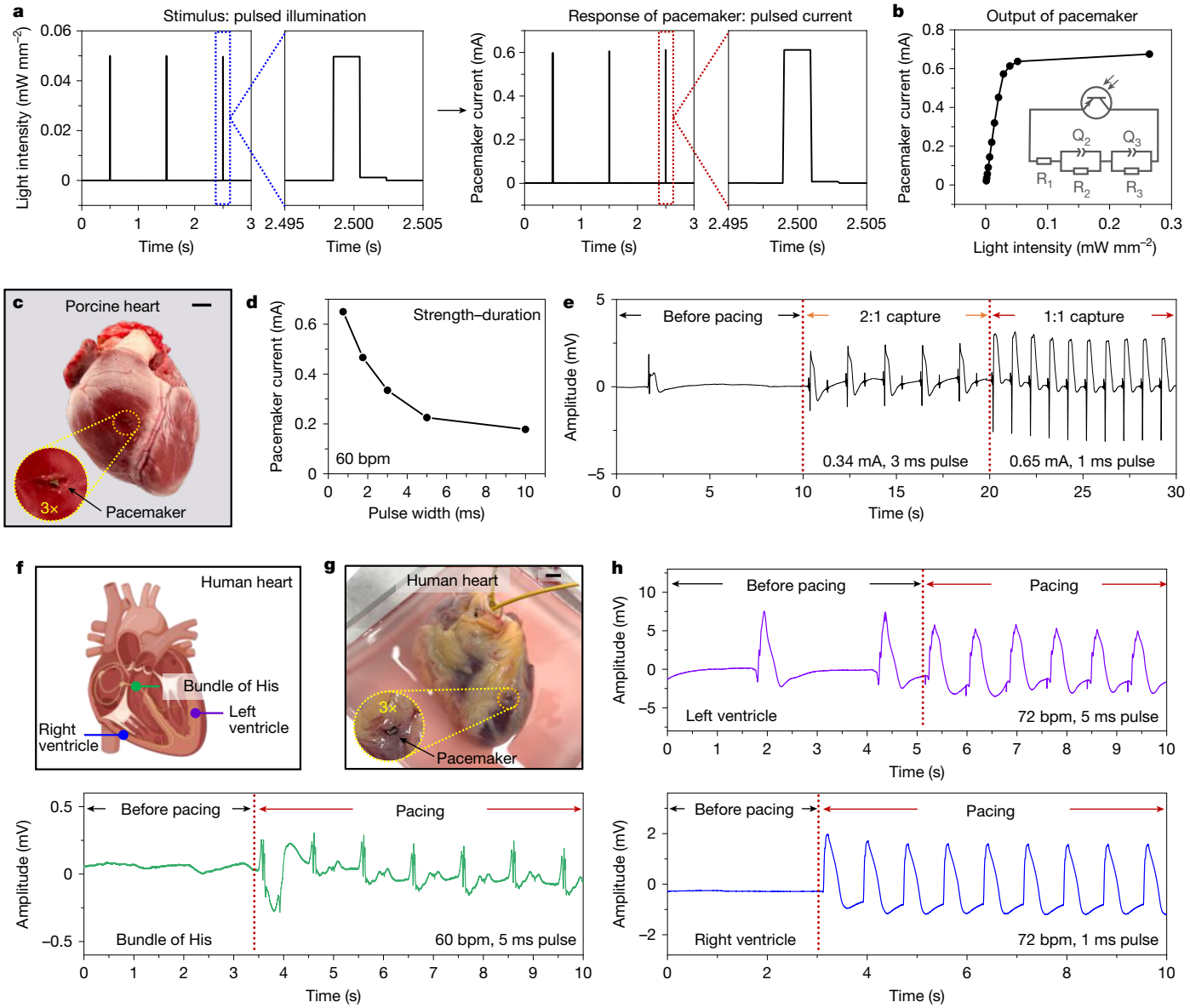

Fig. 2 | Optoelectronic characteristics and ex vivo pacing with human and porcine hearts. a, Temporal response of a pacemaker under pulsed light illumination. **b**, Output currents of a pacemaker as a function of light intensity. Inset: equivalent circuit of the pacemaker. R_1, ohmic resistance; R_2, charge transfer resistance of the anode; R_3, charge transfer resistance of the cathode; Q_2, constant phase element of the anode; Q_3, constant phase element of the cathode. **c**–**e**, Photograph (**c**), strength–duration curve (**d**) and ECG results (**e**) of ex vivo porcine heart pacing. $n = 3$ biologically independent animals. **f**–**h**, Schematic illustration (**f**), photograph (**g**) and ECG results (**h**) of ex vivo human heart pacing at three different sites: left ventricle, right ventricle and bundle of His. $n = 5$ biologically independent individuals. Scale bars, 1 cm (**c** and **g**). Illustration of the heart in **f** was created with BioRender (https://biorender.com).

at a current twice that of the rheobase are about 0.18 mA and about 2.8 ms, respectively. This curve confirms that the pacemaker can achieve more than twice the threshold, ensuring reliable operation post-implantation. Figure 2e shows ECG recordings before and during pacing with 2:1 and 1:1 captures at different pacing conditions. Additional experiments demonstrate successful pacing on human hearts (Fig. 2f–h) at three different sites, including left ventricle, right ventricle and bundle of His. These data demonstrate the potential for multi-site resynchronization therapy or physiological pacing in patients with heart failure who suffer from asynchronous electrical excitation and, therefore, suboptimal mechanical contraction, leading to reduced cardiac output. Discharge profiles of the Mg–MoO_3 pacing pairs (Extended Data Fig. 3 and Supplementary Note 5) in agarose gel at 37 °C indicate an ability to operate continuously for about 16 days at currents, rates, and pulse widths of about 0.4–0.5 mA, 60 bpm and 5 ms, respectively. These parameters exceed requirements in temporary pacing[30].

In vivo injection and closed-chest pacing

Envisioned clinical uses of the technology involve illumination through the skin. Monte Carlo analysis[31–36] (Fig. 3a) captures the distribution of normalized intensity of NIR light (850 nm) in the human body associated with light emitted from an area of 4.96 × 4.96 cm^2 at the surface of the chest. Figure 3b shows that the ribs block more light than the soft tissue. Owing to strong light scattering within the body, differences between areas underneath the ribs and soft tissues become less pronounced with increased depth. Figure 3c shows both the simulation and the experimental results for normalized light intensities on the surface of the phototransistor implanted in the tissue. The simulation results

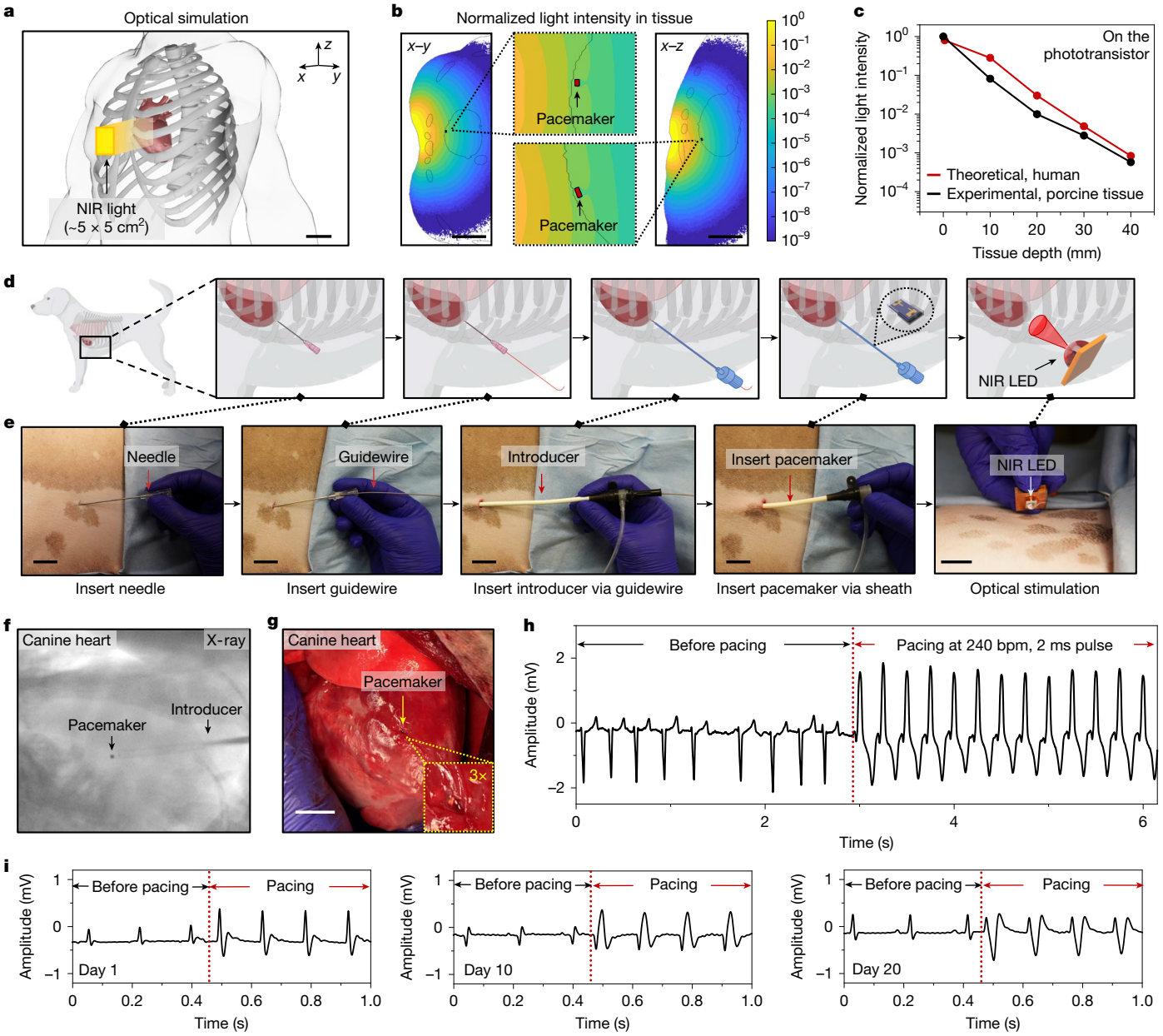

Fig. 3 | In vivo demonstration of pacemaker injection and closed-chest pacing in canine model. a,**b**, Optical simulation showing the normalized light intensity in the body (**b**) when illuminating the skin of the chest with NIR light (850 nm; **a**). **c**, Percentage of light received by the phototransistor at various depths beneath the skin. **d**,**e**, Schematic illustrations (**d**) and photographs (**e**) showing pacemaker injection and optical stimulation. **f**,**g**, Fluoroscopy imaging (**f**; left lateral fluoroscopic view) and photograph (**g**) of a canine heart with a pacemaker inserted in the superficial subepicardial layers of the myocardium. **h**, ECG results before and during cardiac pacing under optical stimulation. $n = 5$ biologically independent animals. **i**, ECG results before and during cardiac pacing after the implantation of the Zn–MoO_3 pacemakers. Tests extended for 20 days. Pulse width, 5 ms; pacing rate, 430 bpm. $n = 4$ biologically independent animals. Scale bars, 5 cm (**a** and **b**), 2 cm (**e**) and 1 cm (**g**). Illustrations of the human body and heart in **a** were created with TurboSquid. Illustrations of the dog, pink syringe tip and blue introducer in **d** were created with BioRender.com (https://biorender.com).

are 28%, 3.0%, 0.49% and 0.08% at tissue depths of 10 mm, 20 mm, 30 mm and 40 mm, respectively. Experimental measurements through porcine tissues show similar trends, that is, 8%, 1%, 0.3% and 0.06% at tissue depths of 10 mm, 20 mm, 30 mm and 40 mm, respectively. For adults, the average shortest distance between the surface of the skin and the surface of the heart is about 30 mm (ref. 37). For a pacemaker implanted at tissue depths of 10 mm, 20 mm, 30 mm and 40 mm, an output current of 0.64 mA can be achieved with light intensities of approximately 0.18 mW mm^{-2}, 1.72 mW mm^{-2}, 10.6 mW mm^{-2} and 61.7 mW mm^{-2} at the surface of the skin, respectively. These values are all well within a safe range for human exposure[38]. Additional simulation results for tissue thicknesses up to 15 cm (Supplementary Fig. 15) and calculations for the maximum permissible exposures for skin safety (Supplementary Note 6) indicate that the device can be reliably implanted at depths of up to about 60 mm in the body. A modified device, with the phototransistor extended closer to the skin and pacing electrodes remaining inserted into the heart, allows for pacing at deeper locations (Supplementary Fig. 16).

In vivo experiments in a clinically relevant canine model (adult hound dogs) follow the successful in vivo cardiac pacing[39] in small-animal (mouse) models (Extended Data Fig. 4). The canine heart anatomy (shape, size and proportions) and electrophysiology closely resemble those of a human. Initial studies demonstrate the feasibility of minimally invasive injection of the pacemaker. Figure 3d,e shows a

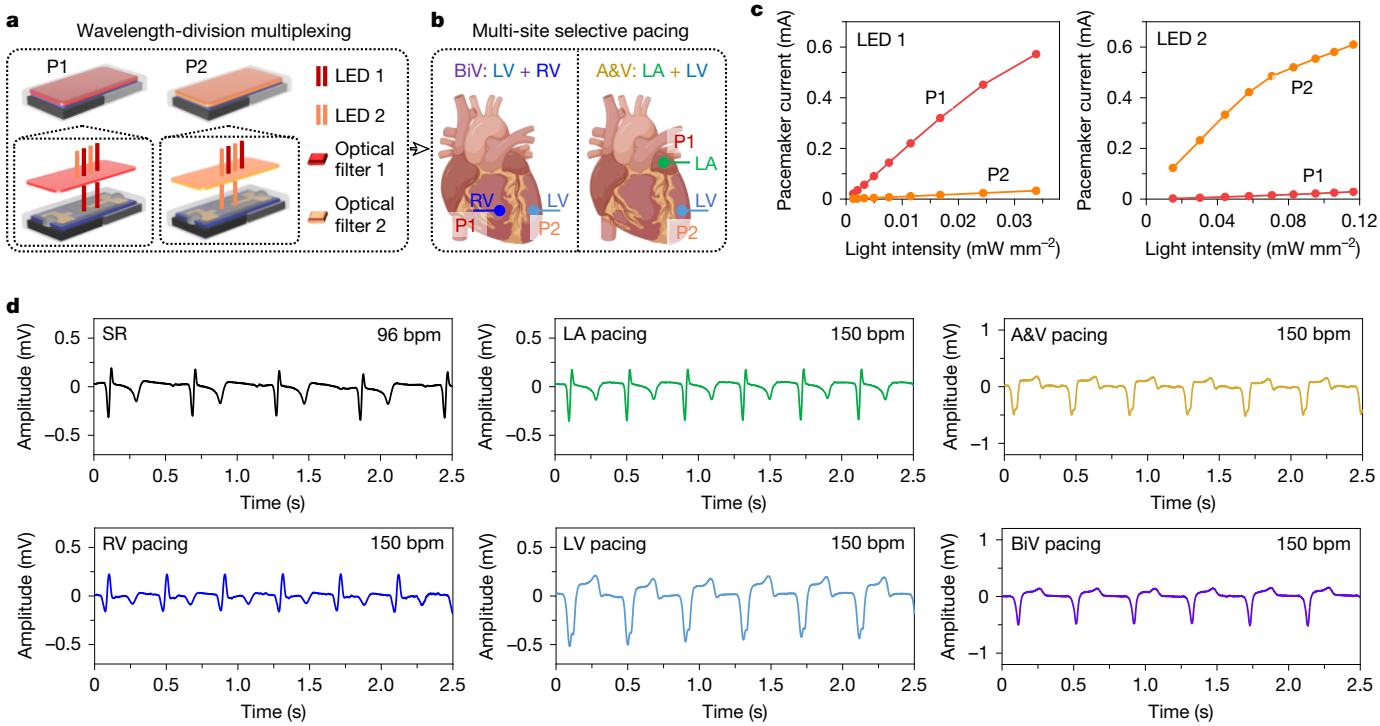

Fig. 4 | In vivo demonstration of multi-site, time-synchronized pacing in canine models. a,**b**, Schematic illustrations of multi-site pacing (**b**) enabled by the WDM control scheme (**a**). Placing two wavelength-selective bioresorbable optical filters atop the phototransistors of two pacemakers ensures independent, wavelength-dependent control over each. **c**, Output currents of pacemakers P1 and P2 during simultaneous illumination at different intensities from LEDs 1 and 2. **d**, ECG (lead I) in sinus rhythm (SR) and during time-synchronized cardiac pacing of sites at 150 bpm, including left atrium (LA) only, left ventricle (LV) only, right ventricle (RV) only, biventricular (BiV; LV + RV, 0 ms LV–RV offset), and dual-chamber (A&V; LA + LV, 80 ms atrioventricular delay). $n = 5$ biologically independent animals. Illustration of the heart in **b** was created with BioRender (https://biorender.com).

schematic outline of the procedure and corresponding intra-operative photographs. Fluoroscopy guides the procedure (Fig. 3f). Direct access via lateral thoracotomy confirms the above procedures (Supplementary Fig. 17) and the position of the pacemaker (Fig. 3g). Locating an NIR light-emitting diode (LED) on the surface of the skin at the sixth intercostal space and activating the LED in a pulsed mode successfully paces the canine heart at 240 bpm. Figure 3h shows an ECG recording with efficient left ventricle pacing and stable 1:1 capture. This technique might benefit from the development of a specialized delivery system to ensure safe and stable placement of the device, such as accessing the pericardial space from the subxiphoid region and fixing the devices through bioresorbable adhesives[40].

In vivo experiments in rat models define the operational lifespan of pacemakers sutured onto the surfaces of the hearts, with the chest cavity closed using surgical procedures described previously[39]. Pulsed light illumination triggers cardiac pacing daily. The results (Fig. 3i and Supplementary Fig. 18) show that pacemakers made of Mg–MoO_3 and Zn–MoO_3 pairs can function in vivo for up to 6 days and 20 days post-implantation, respectively. This timescale exceeds requirements in temporary pacing with an average duration of 4.2 days[30]. Pacing thresholds rise significantly from day 2 for the Mg–MoO_3 and from day 19 for the Zn–MoO_3 pair, possibly owing to the combined effects of local inflammation and electrode degradation.

Time-synchronized multi-site pacing

Programmable optoelectronic control of multiple pacemakers forms the basis for time-synchronized multi-site operation for biventricular and dual-chamber pacing (Fig. 4a,b). Narrow-band optical filters (bioresorbable multilayer stacks of SiN_x/SiO_x) placed atop the phototransistors allow for a WDM control scheme, to avoid the need for careful selective illumination of spatially separated devices. Specifically, independent operation relies on illumination at wavelengths aligned with the transmission properties of the filters (Extended Data Fig. 5). LEDs *X*, filters *X* and pacemakers P*X* form a matched group (where $X = 1$ or $X = 2$; Supplementary Notes 7 and 8). As shown in Fig. 4c, the current of the matched pacemaker is more than 17 and more than 20 times that of the unmatched ones, for illumination from LEDs 1 and 2, respectively. This behaviour ensures reliable programmability of cardiac pacing at multiple sites, with timing precisely controlled by the operation of the LEDs.

In vivo experiments in a canine model confirm the feasibility of this approach to multi-site pacing, further facilitated by the small sizes of the devices. Lateral thoracotomy provides access to the heart for the placement of pacemakers. Placing the two pacemakers (P1 and P2) on the right ventricle anterior wall and left ventricle lateral wall allows for biventricular pacing. Positioning at the left atrium lateral wall and left ventricle lateral wall enables dual-chamber pacing (Fig. 4b and Supplementary Fig. 19). Figure 4d and Supplementary Figs. 20–24 present ECG recordings of the intrinsic sinus rhythm (about 96 beats per minute (bpm)) and of different pacing modes at 150 bpm. Initial tests confirm the ability to pace each site separately (right ventricle, left ventricle, left atrium) via illumination with a single LED. Programmable control of both LEDs enables biventricular and dual-chamber pacing. Biventricular pacing with 0 ms left ventricle–right ventricle pacing offset results in narrowing of the QRS complex (85 ± 3 ms) compared with right-ventricle-only (98 ± 3 ms, $P = 0.00025$) or left-ventricle-only (106 ± 2 ms, $P = 0.00001$) pacing. This demonstrates the potential for cardiac resynchronization therapy, an important treatment modality for patients with congestive heart failure caused by dyssynchronous ventricular activation[41]. The top-right panel in Fig. 4d shows successful dual-chamber, left atrium–left ventricle pacing, tested at 80 ms atrioventricular delay. At 120-ms atrioventricular delay (Supplementary Fig. 24), the ECG shows fused QRS complexes owing to partial activation

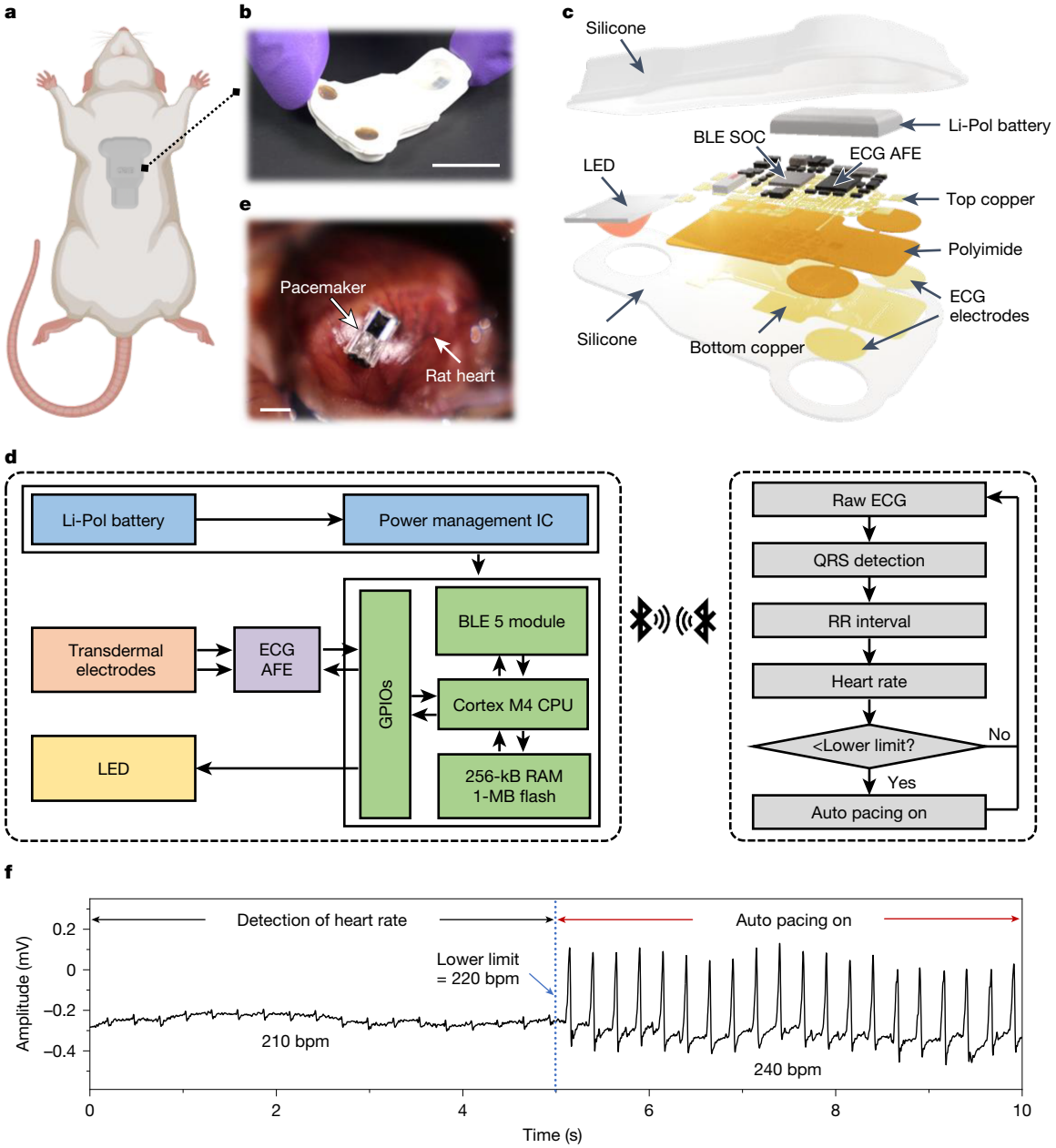

Fig. 5 | Design of a wireless, skin-interfaced optoelectronic system for closed-loop cardiac electrotherapy. a, Schematic illustration of the placement of a soft, skin-interfaced device for monitoring and control in a rat model. **b**,**c**, Photograph (**b**) and exploded view illustration (**c**) of the device. **d**, Architecture of the device, including power management integrated circuits (ICs), a lithium polymer (Li-Pol) battery, a Bluetooth-low-energy (BLE) system-on-a-chip (SOC), an analogue front-end (AFE), ECG sensor, and LED stimulators. CPU, central processing unit; RAM, random access memory; RR interval, the time between two consecutive R-wave peaks. **e**, Photograph showing a pacemaker placed on the surface of a rat heart. **f**, ECG results showing that detection of a heart rate lower than the bradycardia threshold (220 bpm) automatically initiates pacing (240 bpm, 2 ms pulse). GPIOs, general-purpose inputs/outputs, Scale bars, 1 cm (**b**) and 2 mm (**e**). Illustration of the rat in **a** was created with BioRender.com (https://biorender.com).

of the ventricles through the His-Purkinje system. Reducing the atrio-ventricular delay to 80 ms results in a QRS morphology consistent with pure left ventricle pacing. This dual-chamber pacing modality yields a physiology more consistent with normal cardiac activation than that associated with simple ventricular pacing[42].

Closed-loop cardiac electrotherapy

As described earlier, pairing the pacemaker with a wireless, skin-interfaced optoelectronic device allows for autonomous, closed-loop cardiac electrotherapy (Fig. 5a). The technology reported here (Fig. 5b–d) supports (1) single-lead recordings of the ECG, (2) wireless data transfer to a graphical user interface on a laptop for real-time data visualization, (3) closed-loop analytics for automated detection of cardiac arrhythmias, and (4) programmed operation of integrated LEDs to activate cardiac pacing. Examples of this combined system used in the context of bradycardia involve rat models with pacemakers fixed on the surfaces of the hearts accessed by lateral thoracotomy (Fig. 5e) with bioresorbable adhesives[40]. As shown in Fig. 5f, detection of bradycardia (threshold of 220 bpm) automatically initiates pacing at 240 bpm. The use of bioresorbable adhesives[40] here demonstrates a method for fixation that is well suited to small hearts, such as those of paediatric patients, as an alternative to injection of devices in the superficial subepicardial layers of the myocardium.

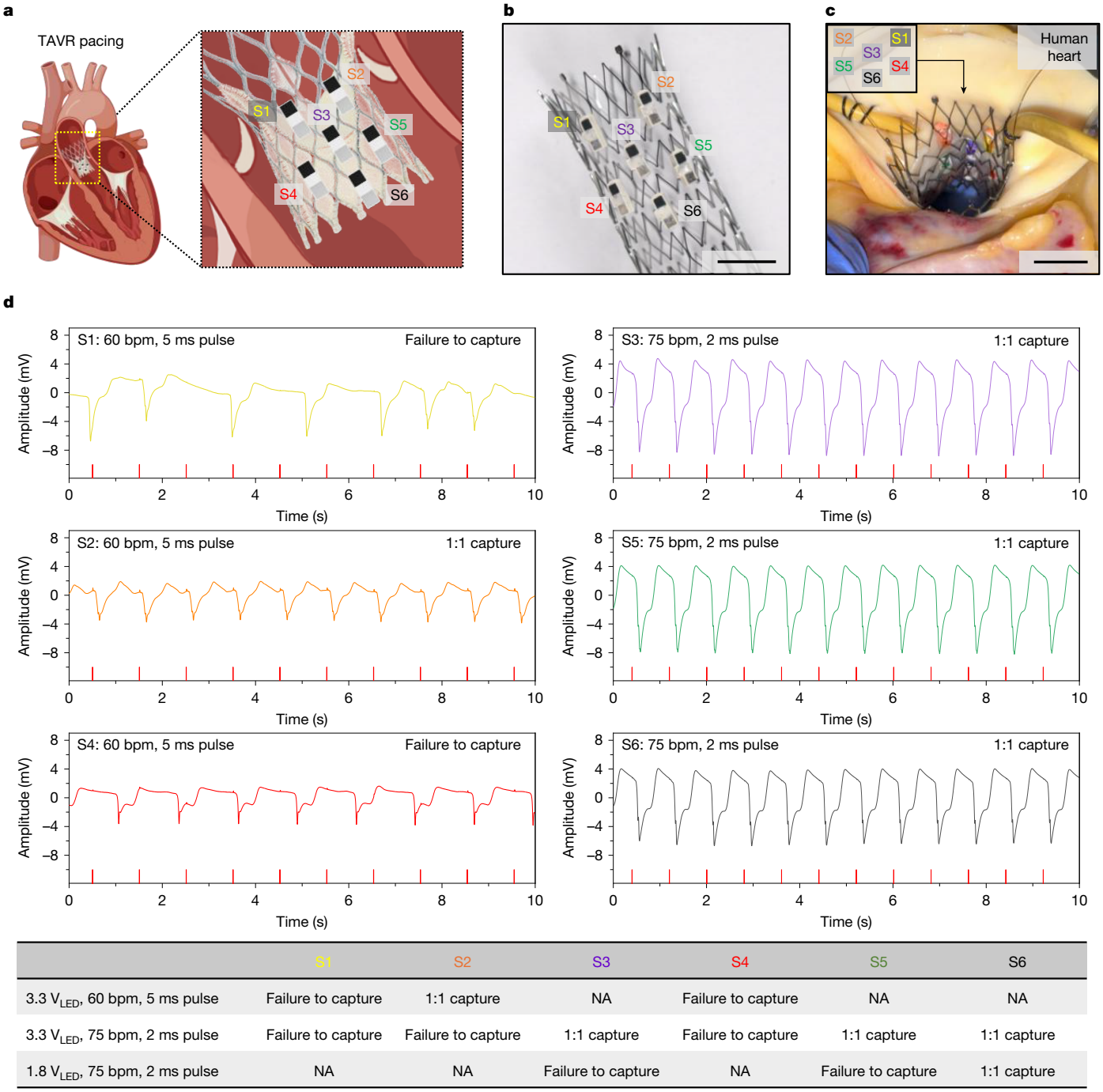

	S1	S2	S3	S4	S5	S6
3.3 V_{LED}, 60 bpm, 5 ms pulse	Failure to capture	1:1 capture	NA	Failure to capture	NA	NA
3.3 V_{LED}, 75 bpm, 2 ms pulse	Failure to capture	Failure to capture	1:1 capture	Failure to capture	1:1 capture	1:1 capture
1.8 V_{LED}, 75 bpm, 2 ms pulse	NA	NA	Failure to capture	NA	Failure to capture	1:1 capture

Fig. 6 | Ex vivo demonstration of cardiac pacing with a collection of pacemakers integrated with a TAVR valve in a human heart. a,**b**, Schematic illustration (**a**) and photograph (**b**) of a deployed TAVR valve mounted with six pacemakers. **c**, Photograph showing the implantation of the valve in the aortic position of a Langendorff-perfused human heart. The pacemakers are colour-coded and their relative locations are shown in the top-left corner. **d**, ECG results during independent activation of each pacemaker. The table at the bottom summarizes the pacing abilities of these pacemakers under different stimulation conditions. NA, not applicable; V_{LED}, voltage applied to the LED. $n = 3$ biologically independent subjects. Scale bars, 1 cm (**b** and **c**). Illustration of the heart in **a** was created with BioRender.com (https://biorender.com).

Pacemaker-integrated TAVR platforms

The widely used TAVR procedure is a minimally invasive replacement of the aortic valve in patients with severe aortic stenosis. Up to 30% of patients with TAVR may, however, develop significant atrioventricular conduction disturbances, thereby necessitating the implantation of a pacemaker with its associated challenges, risks and costs[43–45]. The miniaturized devices introduced here offer a unique solution to this problem, through their direct, simple integration with the frame system used in the TAVR process (Fig. 6a), in a manner that requires minimal change in the surgical procedure. This technique can address temporary conduction disturbances and provide more time to determine whether permanent pacemakers are necessary. Collections of such integrated devices can deliver regular pacing during the post-operative period. Supplementary Note 9 describes the pacing technique during TAVR implantation. This function reduces patient risks and exposures to potential complications, simplifies the procedure, refines the post-operative care process, and allows safe and early patient discharge[46,47].

Experiments show that this integrated device placed in the area of the aortic annulus can effectively capture the ventricular myocardium in the ex vivo Langendorff-perfused human heart model (Supplementary Fig. 25). The system consists of six independent pacemakers mounted on the junction points of the struts of a self-expanding stent (BD Venovo Venous Stent System), a TAVR frame, as shown in Fig. 6b. Deployment into the aortic annulus area occurs with conventional delivery apparatus (Fig. 6c). Placing pacemakers with electrodes facing the septal wall allows for effective pacing of the myocardium. Orienting most of the electrodes towards the antero-septal region of the left ventricle ensures proximity to the heart conduction system. Supplementary Note 10 discusses the illumination strategy. Feasibility tests use fibre-coupled LEDs to activate each pacemaker separately, starting from lower intensities, faster pacing rates and shorter pulse widths, followed by adjusting these parameters across a range until 100% capture, or failure. Figure 6d shows ECG recordings upon independent activation of each pacemaker. Pacemakers S2, S3, S5 and S6 produce reliable 100% capture, with pacing effectiveness S6 > S3 ≈ S5 > S2, considering the conditions required for successful pacing as shown in the table at the bottom of Fig. 6d. Pacemakers S1 and S4 located on the same edge of the stent fail to capture, probably owing to their unfavourable locations—far from the conduction system (Supplementary Fig. 26). A plurality of pacemakers integrated in this manner and activated simultaneously by external flood illumination ensures reliable pacing even when the orientation and precise positioning of the TAVR valve cannot be controlled during implantation.

Discussion

The millimetre-scale, bioresorbable optoelectronic system introduced here represents a unique class of pacing technology capable of broad applications as injectable, wireless sources of electrostimulation. This technology relies on significant differences in the underlying concepts, in the engineering parameters and the clinical use cases compared with previously reported bioresorbable electrostimulators (Supplementary Note 11 and Supplementary Tables 2 and 3). Broad experimental and computational studies reveal the fundamental aspects of the materials science, device operation and clinical uses, the latter through optically controlled cardiac pacing in small- and large-animal models. Options for minimally invasive implantation techniques represent key features of particular value for all paediatric patients and for many adults for whom conventional, wired technologies are poorly suited. The minimized device load on and risks to the patient are also important in delivering improved outcomes. The capabilities for multi-site pacing for collections of devices follow naturally from concepts in WDM, as the basis for advanced pacing modalities such as biventricular pacing for cardiac resynchronization therapy and dual-chamber pacing for physiologically consistent responses. Compatibility with magnetic resonance imaging and computed tomography imaging methods allows for opportunities in advanced diagnotherapy.

Many of these engineering attributes create unique strategies, such as integration with established medical implants or temporary devices. As a specific example, the results show that collections of devices bonded at locations distributed across TAVR frames offer the potential for managing post-procedural TAVR conduction disturbances, such as the atrioventricular block. Successful clinical application in this context could enable same-day discharge of patients for an ambulatory procedure that, in its current form, requires intensive-care-unit settings[47,48]. This concept foreshadows an era of cardiac care where structural and electrical support converge in a single minimally invasive procedure with seamless, patient-centric intervention, activated on demand.

The base technology can be readily adapted for a broad range of additional applications in electrotherapy. Areas of particular interest are electrical stimulation for nerve and bone regeneration, wound therapy, skeletal muscle stimulation, and pain management. Promising directions for future research in these and other areas include means for further miniaturization through materials and device design optimization, for introduction of stimulus-responsive materials for actively controlled degradation, for investigation of other mechanisms for wireless control, for enhanced safety in surgical delivery, and for improved fixation of devices through bioresorbable adhesives[40] for relatively small hearts. Important additional opportunities are in advanced clinical application of this technology and integration of this approach with other medical procedures.

Online content

Any methods, additional references, Nature Portfolio reporting summaries, source data, extended data, supplementary information, acknowledgements, peer review information; details of author contributions and competing interests; and statements of data and code availability are available at https://doi.org/10.1038/s41586-025-08726-4.

1. Choi, Y. S. et al. Fully implantable and bioresorbable cardiac pacemakers without leads or batteries. *Nat. Biotechnol.* **39**, 1228–1238 (2021).
2. Zhang, Y. et al. Advances in bioresorbable materials and electronics. *Chem. Rev.* **123**, 11722–11773 (2023).
3. Choi, Y. S. et al. A transient, closed-loop network of wireless, body-integrated devices for autonomous electrotherapy. *Science* **376**, 1006–1012 (2022).
4. Lumia, F. J. & Rios, J. C. Temporary transvenous pacemaker therapy: an analysis of complications. *Chest* **64**, 604–608 (1973).
5. Wood, M. A. & Ellenbogen, K. A. Cardiac pacemakers from the patient's perspective. *Circulation* **105**, 2136–2138 (2002).
6. Bar-Cohen, Y. et al. Minimally invasive implantation of a micropacemaker into the pericardial space. *Circ. Arrhythm. Electrophysiol.* **11**, e006307 (2018).
7. Zhao, J. et al. Permanent epicardial pacing in neonates and infants less than 1 year old: 12-year experience at a single center. *Transl. Pediatr.* **11**, 825–833 (2022).
8. Wildbolz, M., Dave, H., Weber, R., Gass, M. & Balmer, C. Pacemaker implantation in neonates and infants: favorable outcomes with epicardial pacing systems. *Pediatr. Cardiol.* **41**, 910–917 (2020).
9. Wilhelm, M. J. et al. Cardiac pacemaker infection: surgical management with and without extracorporeal circulation. *Ann. Thorac. Surg.* **64**, 1707–1712 (1997).
10. Donovan, K. D. & Lee, K. Y. Indications for and complications of temporary transvenous cardiac pacing. *Anaesth. Intensive Care* **13**, 63–70 (1985).
11. BRAUN, M. U. et al. Percutaneous lead implantation connected to an external device in stimulation-dependent patients with systemic infection—a prospective and controlled study. *Pacing Clin. Electrophysiol.* **29**, 875–879 (2006).
12. Ouyang, H. et al. Symbiotic cardiac pacemaker. *Nat. Commun.* **10**, 1821 (2019).
13. Lyu, H. et al. Synchronized biventricular heart pacing in a closed-chest porcine model based on wirelessly powered leadless pacemakers. *Sci. Rep.* **10**, 2067 (2020).
14. Ho, J. S. et al. Wireless power transfer to deep-tissue microimplants. *Proc. Natl Acad. Sci. USA* **111**, 7974–7979 (2014).
15. Wang, S. et al. A self-assembled implantable microtubular pacemaker for wireless cardiac electrotherapy. *Sci. Adv.* **9**, eadj0540 (2023).
16. Prominski, A. et al. Porosity-based heterojunctions enable leadless optoelectronic modulation of tissues. *Nat. Mater.* **21**, 647–655 (2022).
17. Liu, Z. et al. Photoelectric cardiac pacing by flexible and degradable amorphous Si radial junction stimulators. *Adv. Healthc. Mater.* **9**, 1901342 (2020).
18. Wang, L. et al. A fully biodegradable and self-electrified device for neuroregenerative medicine. *Sci. Adv.* **6**, eabc6686 (2020).
19. Zhang, Y. et al. Self-powered, light-controlled, bioresorbable platforms for programmed drug delivery. *Proc. Natl. Acad. Sci. USA* **120**, e2217734120 (2023).
20. Huang, I. et al. High performance dual-electrolyte magnesium–iodine batteries that can harmlessly resorb in the environment or in the body. *Energy Environ. Sci.* **15**, 4095–4108 (2022).
21. Won, S. M. et al. Natural wax for transient electronics. *Adv. Funct. Mater.* **28**, 1801819 (2018).
22. Choi, Y. S. et al. Biodegradable polyanhydrides as encapsulation layers for transient electronics. *Adv. Funct. Mater.* **30**, 2000941 (2020).
23. Song, G. Control of biodegradation of biocompatable magnesium alloys. *Corros. Sci.* **49**, 1696–1701 (2007).
24. Schauer, A. et al. Biocompatibility and degradation behavior of molybdenum in an in vivo rat model. *Materials* **14**, 7776 (2021).
25. Yin, L. et al. Dissolvable metals for transient electronics. *Adv. Funct. Mater.* **24**, 645–658 (2014).
26. Yu, K. J. et al. Bioresorbable silicon electronics for transient spatiotemporal mapping of electrical activity from the cerebral cortex. *Nat. Mater.* **15**, 782–791 (2016).
27. Kang, S.-K. et al. Bioresorbable silicon electronic sensors for the brain. *Nature* **530**, 71–76 (2016).
28. Li, G. et al. Flexible transient phototransistors by use of wafer-compatible transferred silicon nanomembranes. *Small* **14**, e1802985 (2018).
29. Li, G. et al. Silicon nanomembrane phototransistor flipped with multifunctional sensors toward smart digital dust. *Sci. Adv.* **6**, eaaz6511 (2020).
30. López Ayerbe, J. et al. Temporary pacemakers: current use and complications. *Rev. Esp. Cardiol. Engl. Ed.* **57**, 1045–1052 (2004).

31. Yu, L., Nina-Paravecino, F., Kaeli, D. & Fang, Q. Scalable and massively parallel Monte Carlo photon transport simulations for heterogeneous computing platforms. *J. Biomed. Opt.* **23**, 1 (2018).
32. Fang, Q. & Boas, D. A. Monte Carlo simulation of photon migration in 3D turbid media accelerated by graphics processing units. *Opt. Express* **17**, 20178 (2009).
33. Taroni, P., Pifferi, A., Torricelli, A., Comelli, D. & Cubeddu, R. In vivo absorption and scattering spectroscopy of biological tissues. *Photochem. Photobiol. Sci.* **2**, 124–129 (2003).
34. Khan, R., Gul, B., Khan, S., Nisar, H. & Ahmad, I. Refractive index of biological tissues: review, measurement techniques, and applications. *Photodiagnosis Photodyn. Ther.* **33**, 102192 (2021).
35. Green, M. A. & Keevers, M. J. Optical properties of intrinsic silicon at 300 K. *Prog. Photovoltaics Res. Appl.* **3**, 189–192 (1995).
36. Firbank, M., Hiraoka, M., Essenpreis, M. & Delpy, D. T. Measurement of the optical properties of the skull in the wavelength range 650–950 nm. *Phys. Med. Biol.* **38**, 503–510 (1993).
37. Rahko, P. S. Evaluation of the skin-to-heart distance in the standing adult by two-dimensional echocardiography. *J. Am. Soc. Echocardiogr.* **21**, 761–764 (2008).
38. Chen, R. et al. Deep brain optogenetics without intracranial surgery. *Nat. Biotechnol.* **39**, 161–164 (2021).
39. Yin, R. T. et al. Open thoracic surgical implantation of cardiac pacemakers in rats. *Nat. Protoc.* **18**, 374–395 (2023).
40. Yang, Q. et al. Photocurable bioresorbable adhesives as functional interfaces between flexible bioelectronic devices and soft biological tissues. *Nat. Mater.* **20**, 1559–1570 (2021).
41. Shea, J. B. & Sweeney, M. O. Cardiac resynchronization therapy a patient's guide. *Circulation* **108**, e64–e66 (2003).
42. Connolly, S. J., Kerr, C., Gent, M. & Yusuf, S. Dual-chamber versus ventricular pacing. *Circulation* **94**, 578–583 (1996).
43. Rodés-Cabau, J., Muntané-Carol, G. & Philippon, F. Managing conduction disturbances after TAVR: toward a tailored strategy. *JACC Cardiovasc. Interv.* **14**, 992–994 (2021).
44. Urena, M. & Rodés-Cabau, J. Conduction abnormalities: the true Achilles' heel of transcatheter aortic valve replacement? *JACC Cardiovasc. Interv.* **9**, 2217–2219 (2016).
45. Pagnesi, M. et al. Incidence, predictors, and prognostic impact of new permanent pacemaker implantation after TAVR with self-expanding valves. *JACC Cardiovasc. Interv.* **16**, 2004–2017 (2023).
46. Reiter, C. et al. Delayed total atrioventricular block after transcatheter aortic valve replacement assessed by implantable loop recorders. *JACC Cardiovasc. Interv.* **14**, 2723–2732 (2021).
47. Muntané-Carol, G. et al. Ambulatory electrocardiographic monitoring following minimalist transcatheter aortic valve replacement. *JACC Cardiovasc. Interv.* **14**, 2711–2722 (2021).
48. Krishnaswamy, A. et al. Feasibility and safety of same-day discharge following transfemoral transcatheter aortic valve replacement. *JACC Cardiovasc. Interv.* **15**, 575–589 (2022).

Methods

Fabrication and characterization of galvanic cells and pacing electrodes

Pacing electrodes used a Mg alloy AZ31 ($Mg_{96}Al_3Zn_1$, 250 μm thick, Goodfellow) or a Zn anode and a MoO_3 cathode. Mixing 0.45 g MoO_3 (Sigma-Aldrich), 0.05 g carbon black (MTI) and 800 μl of 300 mg ml^{-1} poly(D,L-lactide-co-glycolide) (PLGA, lactide:glycolide 65:35, molecular weight (M_w) 40,000–75,000, Sigma-Aldrich) in ethyl acetate within a planetary mixer (Thinky ARE-30) yielded a slurry for the MoO_3/C cathode. Mixing 0.9 g MoO_3, 0.9 g Mo powder (Sigma-Aldrich, size 1–5 μm) and 900 μl of 200 mg ml^{-1} PLGA in ethyl acetate formed a MoO_3/Mo slurry. Mo gauze (40 mesh, Alfa Aesar) or Mo foil (5 μm thick, Goodfellow) served as current collectors for the cathode materials. Applying the slurries on these current collectors and baking at 80 °C for 1 h completed the process. Mixing 0.5 g Zn powder (Sigma-Aldrich, size 40–60 nm), 0.04 g carbon black and 800 μl of 300 mg ml^{-1} PLGA in ethyl acetate formed a Zn slurry. Zn foil (50 μm thick, Goodfellow) served as current collectors for the Zn anode materials. The Zn slurry was applied on both sides of the Zn current collectors, followed by baking at 120 °C for 50 min. The Zn anodes were then sintered in 5 wt% acetic acid aqueous solution at room temperature for 30 min and dried in the air. An ultraviolet laser prototyping system (LPKF U4) defined the shapes of the Mg-alloy anodes, Zn anodes and MoO_3 cathodes from Mg-alloy AZ31 foil, Zn foil, Mo foil and Mo gauze. The discharge behaviours in phosphate-buffered saline electrolyte were tested under constant-current discharge using a Landt battery tester. Electrochemical impedance spectroscopy under potentiostatic mode relied on a Metrohm system, using a frequency range of 500 kHz to 0.1 Hz, with a voltage amplitude of 10 mV.

Fabrication and characterization of phototransistors

Thin (100) Si wafers (100 μm thick; boron doped; 1–10 Ω cm) were cleaned with standard cleaning (SC) procedures defined by Radio Corporation of America (RCA) including SC-1 (NH_4OH:H_2O_2:H_2O = 1:1:5) and SC-2 (HCl:H_2O_2:H_2O = 1:1:6). Dry oxidation at 1,000 °C for 7 h formed a 200-nm-thick oxide layer as a mask for the doping process. Photolithographic patterns defined base-doping regions (that is, the photosensitive region of the phototransistor) and a combination of CH_4/O_2 dry etching and 6:1 buffered oxide etchant (BOE) wet-etching processes removed the oxide layer to expose areas for base (n) doping. After cleaning the wafer again with SC-1 and SC-2, 120-keV phosphorus ions were implanted with a dose of 6×10^{12} ions per cm^2 into Si to form the n base area. The remaining oxide mask was removed in BOE (6:1), followed by dry oxidation at 1,000 °C for 7 h to activate implanted ion dopants and create a second oxide mask. Photolithographic patterns defined each doping region for the emitter and the collector electrode, respectively. After RCA cleaning again, highly concentrated boron doping (p^+) was performed in a tube furnace with a solid boron source at 1,000 °C for 20 min under a nitrogen atmosphere. The remaining oxide mask was removed in BOE (6:1), followed by 100-nm-thick SiO_2 deposition using plasma-enhanced chemical vapour deposition (PECVD) to fully encapsulate bipolar-junction-transistor-based phototransistors. Photolithographic patterns defined metal contact holes for the emitter (E) and collector (C) area. The exposed SiO_2 layer was removed in BOE (6:1) to open contact areas for E/C metals. E/C metal electrodes were patterned with AZ nLoF 2035, followed by sputter deposition of tungsten (100 nm thick) and lift-off in acetone. A laser cutting system defined the rectangular geometries of the phototransistors. Mechanical polishing processes thinned the phototransistors (down to approximately 10 μm thick). The characteristic responses of the phototransistors under various light intensities were determined by linear sweep voltammetry using a PalmSens4 system.

Fabrication and characterization of optical filters

Alternating SiO_x and SiN_y layers were deposited onto 100-μm-thick Si substrates using PECVD. Drop-casting PLGA (lactide:glycolide 65:35, M_w 40,000–75,000, Sigma-Aldrich) solution (7 wt% in ethyl acetate) on the above multilayers and baking at 70 °C yielded 10-μm-thick PLGA films attached to the multilayers. Etching the Si substrates from the backside under a vapour of XeF_2 completed the fabrication. The Perkin Elmer LAMBDA 1050 spectrophotometer measured the transmission spectra of the filters. A Thorlabs' PM200 Optical Power and Energy Meter recorded the intensities of light from LEDs (Digi-Key; LED 1, LZ4-00R408; LED 2, MTPS7065MT2-BK) before and after passing through the filters.

Fabrication and characterization of pacemakers

Bioresorbable pacing electrodes including a Mg-alloy AZ31 or a Zn composite anode and a MoO_3 cathode were electrically connected to a bioresorbable phototransistor through a biodegradable conductive paste (Candelilla wax/W powder)[21]. Bioresorbable optical filters placed atop the phototransistors provided a wavelength-selective response. Polybutanedithiol 1,3,5-triallyl-1,3,5-triazine-2,4,6(1*H*,3*H*,5*H*)-trione pentanoic anhydride (polyanhydride)[22] or a mixture of natural wax (candelilla wax and beeswax, mass ratio 3:2)[21] served as the encapsulation material (total size of 3.5 mm × 1.8 mm × 1 mm). To measure the output current of a pacemaker in tissue under pulsed light, the pacing electrodes (placed within tissue), the phototransistor and a current measurement module (National Instruments CompactDAQ NI-9208, configured in reference single-ended mode) were electrically connected in series. A function generator (Rigol) powered the LEDs and generated pulsed light with various light intensities on the phototransistor.

Optical control systems for activation of pacemakers

Supplementary Note 7 lists the detailed parameters for the LEDs used in this work. The SparkFun FemtoBuck LED Driver served as a mechanism to control the LEDs. Replacing the sense resistor of the internal AL8860 d.c.–d.c. step-down converter of the LED driver with a 0.05-Ω shunt resistor bypassed the low default output (330 mA) and enabled a nominal average output of up to 2 A.

Finite element analysis

The three-dimensional finite element analysis used commercial software (Ansys Maxwell) to define the distributions of current density in the heart under electrical stimulation. Use of an adaptive mesh (tetrahedron elements) ensured computational accuracy. The pacemaker was inserted 1 mm deep into a three-dimensional heart model (TurboSquid). The relative permittivity (ε_r) and bulk conductivity (σ) were 2.36×10^7 and 0.0537 S m^{-1} for the heart tissue, 12.6 and 2.3 S m^{-1} for the MoO_3 composite, and 3 and 6.7×10^{-16} S m^{-1} for polyanhydride. The electromagnetic parameters of other materials relied on the material library in the Ansys Maxwell software package.

Optical simulation

The Monte Carlo method was used to simulate the light transport within the human body[31,32]. The body, with bones and the heart, was voxelated, creating a simulation space of 700 × 200 × 566 voxels, each with a side length of 0.62 mm. A total of 5×10^9 photons were simulated to ensure accuracy. The light was passed through the front of the body across a square region of 4.96 cm × 4.96 cm, with the incident direction along the negative axis. The light has a wavelength of 850 nm. The absorption coefficient (μ_a) and the reduced scattering coefficient (μ_s') are 0.03 mm^{-1} and 1.8 mm^{-1} for bones[36], and 0.006 mm^{-1} and 1.3 mm^{-1} for other tissues[33]. The refractive indices (n)[34] for all tissues are 1.4. In addition, a pacemaker occupying 3 × 2 × 5 voxels was placed in the heart wall, with μ_a = 53.5 mm^{-1}, μ_s' = 0 mm^{-1} and n = 3.65 (ref. 35).

Fabrication and operation of the soft, skin-interfaced optoelectronic controller

Electrical components. The system was assembled on a double-layer flexible printed circuit board (copper (18 μm): polyimide (75 μm): copper (18 μm)). A lithium polymer battery (PowerStream Technology) powered the device. The output voltage of the battery was converted to a constant voltage (2.5 V) by a low-dropout linear voltage regulator (ADP7112, Analog Devices) in a 6-pin wafer-level chip-scale package (1.2 mm × 1 mm) to power the system. A BLE SOC (nRF52832-CIAA, Nordic Semiconductor) with a footprint of 3.0 mm × 3.2 mm served as the microcontroller and wireless communication module. An ultralow-power (180 μW), high common-mode rejection (>100 dB) biopotential AFE (MAX30003, Analog Devices) with a footprint of 2.74 mm × 2.9 mm amplified, filtered and digitized the ECG signal and transmitted the digital data to the BLE SOC via the serial peripheral interface. The BLE SOC streamed the ECG signal in real time to a custom Python script on a laptop. The BLE SOC directly controlled the LEDs via general-purpose inputs/outputs. The BLE SOC used a miniaturized (3.2 mm × 1.6 mm) ceramic 2.45-GHz antenna (2450AT18A100, Johanson Technology). Passive components with the smallest packaging, such as 0201 (imperial), were used to minimize the overall size of the system.

Assembly and encapsulation of the device. Electrical components were soldered to the flexible printed circuit board by hot-air soldering. An epoxy adhesive (Loctite 3621, Henkel) was applied to the BLE SOC and MAX30003 and cured at 95 °C for 25 min to provide mechanical protection for the chips. Casting of a silicone gel (Silbione RT GEL 4717 A&B, Elkem) into the gap between the milled aluminium core and cavity moulds (Roland MDX 540) and curing at 75 °C for 90 min formed the top encapsulation layer. Spin-coating of the silicone gel on a thin acrylic plate at 180 rpm for 1 min and curing at 75 °C for 90 min formed the bottom encapsulation layer. Filling the cavity between the top and bottom encapsulation layers with Ecoflex 0030 and curing at 60 °C for 30 min ensured full coverage of the components.

Data collection and data analysis. The ECG data were collected at 512 Hz. Custom Python code with Python 3.8.10 and Bleak 0.12.1, Scipy 1.7.3, Numpy 1.20.2, Pandas 1.2.5 and Matplotlib 3.3.4 was used to receive and analyse the ECG data. The algorithm analysed the latest 1-s ECG data every 1 s. For each 1-s window, the algorithm started with a Butterworth low-pass filter (cut-off 50 Hz, order 4) to remove high-frequency noise, followed by finding QRS complexes using the find_peaks function of Scipy. Peaks were rejected if the corresponding RR intervals (the time between two consecutive R-wave peaks) were not within ±30% of the mean of the RR intervals of the window. Next, the heart rate of the window was calculated based on the mean of valid RR intervals. If the heart rate was below the threshold, the Python script sends a command with predefined pacing rate and duty cycle to the BLE SOC. The BLE SOC subsequently drives the LED following the parameters in the command.

In vivo demonstration of cardiac pacing in small-animal models

All experimental animal procedures and protocols were approved by the Northwestern University Institutional Animal Care and Use Committee and in compliance with suggestions from the panel of Euthanasia of the American Veterinary Medical Association and the National Institutes of Health Guide for the Care and Use of Laboratory Animals. The in vivo rodent study was performed on mice (15–25 weeks old; C57BL/6J; Jackson Laboratory; male and female) and rats (12–14 weeks old; Sprague–Dawley; Charles Rivers Laboratory; male). The procedure for pacemaker implantation via open thoracotomy was adapted from the standard technique in a previous report[39]. All procedures were performed under general anaesthesia using inhaled isoflurane vapour (1–3%). The animal was ventilated using a VentElite Small Animal Ventilator (Harvard Apparatus). Subdermal ECG leads were connected for intra-operative cardiac monitoring (lead II configuration) using PowerLab 4/26 and PowerLab FE234 Quad Bio Amp and LabChart ECG Recording software (ADInstruments). The heart was exposed via left thoracotomy.

In acute studies, the pacemaker was secured (with the electrode side facing down) onto the epicardial surface using non-absorbable monofilament 6-0 polypropylene suture (Ethicon, 8705H) or photocurable bioresorbable adhesives[40]. In long-term studies, steroids (15 mg dexamethasone acetate, Sigma) were added into 800 μl of 300 mg ml^{-1} PLGA in ethyl acetate while fabricating Zn and MoO_3 composite electrodes. The photocurable hydrogel[40] was applied on the surfaces of the electrodes, followed by curing under ultraviolet light. Pacemakers were sterilized in an ethylene oxide sterilizer (AN74i sterilizer) for 24 h before implantation. The pacemaker was sutured onto the epicardial surface using non-absorbable monofilament 6-0 polypropylene suture (Ethicon, 8705H). After surgical implantation, pacemakers were tested daily. Illuminating the anterior chest with an NIR LED activated the pacemaker. The illumination intensity, frequency and duty cycle controlled the current, rate and pulse width of the pacing process, respectively. The minimum voltage required to successfully pace the heart was recorded as the pacing threshold. Local inflammation can lead to a significant increase in the threshold following the implantation of the pacemaker. Therefore, maintaining a safety margin of at least two times the sensing threshold is necessary to ensure stable and reliable operation, a standard practice in clinical settings to counteract post-implantation threshold increases.

Ex vivo demonstration of cardiac pacing with the whole human and porcine hearts

Donor human hearts rejected for organ transplant were procured from the Gift of Hope Organ & Tissue Donor Network as deidentified discarded tissue not involving human individuals. Porcine hearts were acquired from the Center of Comparative Medicine of Northwestern University as post-euthanasia tissue transfer. At the time of tissue procurement, the left and right coronary arteries of the heart were perfused with cold University of Wisconsin cardioplegic solution and were then cannulated separately. The heart was then transferred to a Langendorff perfusion system with a custom tissue chamber and was perfused with a modified Tyrode's solution (128.2 mM NaCl, 4.7 mM KCl, 1.05 mM $MgCl_2$, 1.3 mM $CaCl_2$, 1.19 mM NaH_2PO_4, 20 mM $NaHCO_3$, 11.1 mM glucose) and bubbled with 95% O_2/5% CO_2. The pressure of the heart was maintained between 60 mm Hg and 80 mm Hg by regulating the perfusion flow rate through roller-pumps. The temperature of the perfusion system was maintained at 37 °C throughout the experiment. Far-field ECG signals were acquired and recorded by using LabChart software (AD Instruments) with two sensing electrodes placed on the myocardium surface and one ground electrode placed in the tissue bath around the heart. For cardiac pacing, a 2-mm dissection was made at an angle to the myocardial surface of the ventricles to create a pocket for the pacemaker insertion with the electrode side facing down and the phototransistor side facing up. For TAVR pacing, mounting six pacemakers with epoxy onto the junctions of the struts of the TAVR valve stent (BD Venovo Venous Stent System) formed the pacemaker-integrated TAVR stent, which was then deployed and expanded in the annulus of the aortic valve with electrode side facing the septal wall and the phototransistor part facing the opposite side to be excited by illumination from a fibre-coupled LED (Thorlabs, M660FP1).

In vivo demonstration of pacemaker injection and cardiac pacing in large-animal models

Retired breeder female and male hound dogs (age 1.6–4.5 years, weight 39–53 kg) used in this study were maintained in accordance with the Guide for the Care and Use of Laboratory Animals published by the US National Institutes of Health (NIH Publication no. 85–23, revised 1996) as approved by the Institutional Animal Care and Use Committee

of Northwestern University. Before surgery, the animals were premedicated with acepromazine (0.01–0.02 mg kg^{-1}) and induced with propofol (3–7 mg kg^{-1}). All experiments were performed under general anaesthesia (inhaled) with isoflurane (1–3%). Adequacy of anaesthesia was assessed by toe pinch and palpebral reflex. Surface electrodes that were applied to the limbs allowed continuous 6-lead ECG recording at a sampling rate of 977 Hz (Prucka CardioLab).

The pacemakers were implanted through lateral thoracotomy or minimally invasive injection approaches. In the lateral thoracotomy, the heart was exposed by pericardiectomy. The pacemakers were placed on the myocardial surface or inserted in the superficial subepicardial layers of the myocardium. The NIR LED was placed above the pacemaker location. For long-range optical stimulation, the chest was closed. The NIR LED was positioned on the skin surface in the projection of the pacemaker location. For the minimally invasive injection approach, an 18-gauge needle (1.27 mm in outer diameter) accessed the border of the heart from the eighth intercostal space, followed by subsequent advancement of a guidewire into the pericardial space. Next, a 9 F percutaneous sheath introducer advanced over the wire and reached the epicardial surface of the left ventricle. A dilator pushed the pacemaker through the sheath, under the guidance of fluoroscopy, until the device reached the surface of the heart and entered a pre-made pocket in the superficial subepicardial layer of the myocardium. Activating an NIR LED on the surface of the skin at the sixth intercostal space (in the projection of the pacemaker device location) paced the heart.

Upon finishing the in vivo portion of the study and after confirming a very deep plane of anaesthesia, the heart was removed. No complications or unscheduled deaths occurred.

In vitro cytocompatibility

In vitro cytocompatibility studies of the pacemaker against mouse cells (L929, ATCC) were performed through the indirect contact method. A mixture of Eagle's minimum essential medium (Gibco, 11095080), 10 vol% fetal bovine serum (Thermo Fisher Scientific) and 1 vol% penicillin–streptomycin (Thermo Fisher Scientific) served as the cell culture medium. Incubating samples in cell medium for 24 h resulted in sample extracts (ISO 10993-12), which were centrifuged at 14,000 rpm for 10 min. Supernatants were 1:100 diluted and added into the cell-seeded wells for 24 h. Cell proliferation was assessed using the CellTiter 96 Aqueous One Solution Cell Proliferation Assay (Promega, G3580). The absorbance of the plate was measured at 490 nm. Blank controls (medium alone without cells) were subtracted from the absorbance values in all assays.

In vivo biocompatibility tests

All procedures were performed in accordance with the ethical standards and protocols of Northwestern University. Each male Sprague–Dawley rat (12–14 weeks) was placed under isoflurane anaesthesia (1–3%), then given pre-operative analgesia (0.5–1.0 mg kg^{-1} buprenorphine). Studies involve a device group ($n = 3$) and a control group of high-density polyethylene (US Food and Drug Administration-approved non-toxic material; $n = 3$), each sutured onto the surface of the heart. Animals were weighed every 3 days to monitor weight loss and health status post-surgery. Blood and heart tissues adjacent to the implants were collected at 1- and 4-week endpoints. Heart tissues were fixed in 10% neutral-buffered formalin and embedded in paraffin. Cross-sectional samples were stained with haematoxylin and eosin for histological analysis.

Reporting summary

Further information on research design is available in the Nature Portfolio Reporting Summary linked to this article.

Data availability

The data supporting the results of this study are present in the paper and Supplementary Information. Source data are provided with this paper.

Code availability

The code for connecting to the device via BLE, recording and analysing ECG data in real time, and configuring the pacing parameters in a closed-loop system is available on Code Ocean at https://codeocean.com/capsule/9406347/tree/v1 (ref. 49).

49. Millimetre-scale, bioresorbable optoelectronic systems for minimally invasive electrotherapy. *Code Ocean* https://codeocean.com/capsule/9406347/tree/v1 (2025).

Acknowledgements We acknowledge support from the Querrey Simpson Institute for Bioelectronics, the Leducq Foundation grant 'Bioelectronics for Neurocardiology' and the NIH grant (NIH R01 HL141470). Y.Z. acknowledges support from the National University of Singapore start-up grant and the AHA's Second Century Early Faculty Independence Award (grant: https://doi.org/10.58275/AHA.23SCEFIA1154076.pc.gr.173925). J. Gong and Z.M. acknowledge the support from AFOSR (grant number FA9550-21-1-0081). We thank E. Dempsey, Q. Ma, N. Ghoreishi-Haack, I. Stepien and S. Han for the help in the biocompatibility study and animal experiment. This work made use of the NUFAB facility of Northwestern University's NUANCE Center, which has received support from the SHyNE Resource (NSF ECCS-2025633), the IIN and Northwestern's MRSEC programme (NSF DMR-1720139). This work was supported by the Developmental Therapeutics Core and the Center for Advanced Molecular Imaging (RRID:SCR_021192) at Northwestern University and the Robert H. Lurie Comprehensive Cancer Center support grant (NCI P30 CA060553).

Author contributions Y.Z. and J.A.R. initiated and conceived the self-powered, light-controlled pacing concept. Y.Z., E.R., I.R.E. and J.A.R. designed the studies and analysed the results. Y.Z., L.Z., K.Z., X.L., A.L., G.J., J.L., F.L., Y.F.L.L., Y.L., C.H., A.H. and R.N. fabricated and characterized the pacemakers. E.R., L.T., A. Mikhailov, L.D., A.B., A.P., A.A. and A. Melisova conducted animal surgeries. Y.Z., E.R., L.Z., L.T., A. Mikhailov, L.D., J.W., A.B., A.P. and W.O., performed in vivo and ex vivo cardiac pacing experiments. W.O., Y.W., J. Gu, T.Y., Y.Y. and Y.L. developed closed-loop and optical control systems. J.U.K., S.G.S., J. Gong, J.J., J.C., S.H.J. and Z.M. designed and fabricated phototransistors. H.Z., S.L., Z.L. and Y.H. performed computational simulations. E.A. and W.B. fabricated bioresorbable optical filters. T.W., N.S.P. and J.M.T. developed and synthesized the hydrogels. L.T., L.D. and K.B. evaluated the biocompatibility. Y.Z., E.R., L.Z., J.U.K., L.T., A. Mikhailov., K.Z., X.L., Y.W., H.Z., A.L., E.A., G.J., S.L., S.G.S., K.B., N.L., W.O., R.K.A., I.R.E. and J.A.R. discussed and interpreted the data. Y.Z. and J.A.R. prepared figures and wrote the paper, with input from E.R., W.O., A. Mikhailov, R.K.A. and I.R.E. In addition, J.U.K., L.Z., L.T., Y.W., H.Z., S.L. and J. Gu. assisted with the preparation of figures and text. Y.Z., L.Z., L.T., H.Z., L.D., W.O., I.R.E. and J.A.R. revised the paper. Y.Z., E.R., L.Z., J.U.K., L.T. and H.Z. contributed equally to this work.

Competing interests The authors declare no competing interests.

Additional information

Supplementary information The online version contains supplementary material available at https://doi.org/10.1038/s41586-025-08726-4.

Correspondence and requests for materials should be addressed to Yamin Zhang, Yonggang Huang, Wei Ouyang, Rishi K. Arora, Igor R. Efimov or John A. Rogers.

Peer review information *Nature* thanks Gábor Duray, Hossam Haick and the other, anonymous, reviewer(s) for their contribution to the peer review of this work. Peer reviewer reports are available.

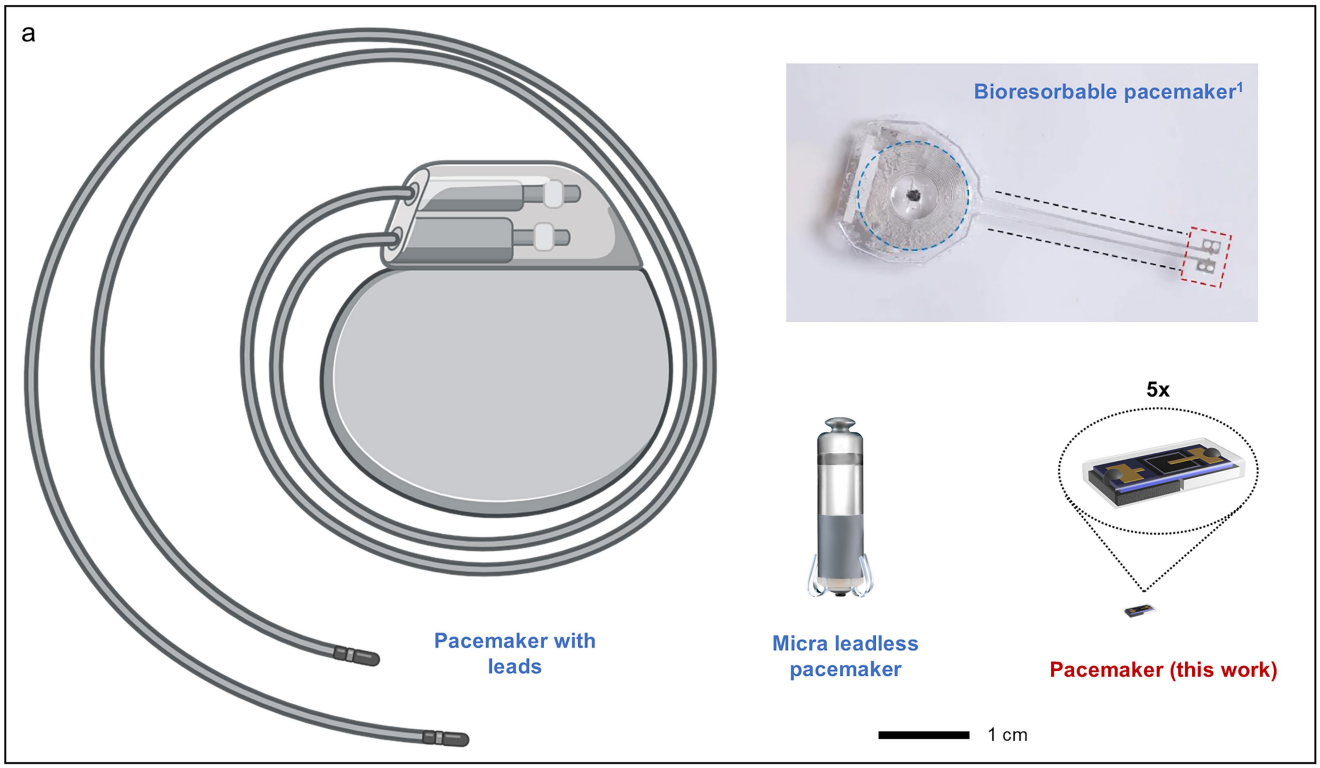

b

Leadless pacemakers	Type	Size	Power supply	Year
Micra pacemaker	Implantable	6.7 mm diameter × 26 mm length	Battery	-
Symbiotic pacemaker[13]	Implantable	~ 61 × 39 × 1 mm^3	TENG	2019
Biventricular pacemaker[14]	Implantable	~ 11 × 11 × 1 mm^3	Wireless RF	2020
Micropacemaker[15]	Implantable	2 mm diameter × 5 mm length	Wireless RF	2014
Micropacemaker[6]	Implantable	5 mm diameter × 24 mm length	Battery	2018
Microtubular pacemaker[16]	Implantable	2.5 mm diameter × 20 mm length	Wireless RF	2023
Optoelectronic pacing[17]	Implantable	~ 5 × 5 × 0.2 mm^3	Photovoltaic	2022
Bioresorbable pacemaker[1]	Implantable and bioresorbable	~ 40 × 15 × 0.25 mm^3	Wireless RF	2021
Photovoltaic pacemaker[18]	Implantable and bioresorbable	~ 15 × 10 × 0.015 mm^3	Photovoltaic	2019
This work	Implantable and bioresorbable	~ 1.8 × 3.5 × 1 mm^3	Self-powered	-

Extended Data Fig. 1 | Comparisons of previously reported pacemakers and the technology introduced here. a, Comparisons between conventional pacemakers with leads, leadless pacemakers, bioresorbable pacemakers, and the pacemaker reported here. **b**, Table showing details of previously reported leadless pacemakers and the pacemaker reported here. Illustration of the pacemaker with leads in **a** was created with BioRender.com (https://biorender.com). Bioresorbable pacemaker in **a** adapted from ref. 1, Springer Nature America, Inc.

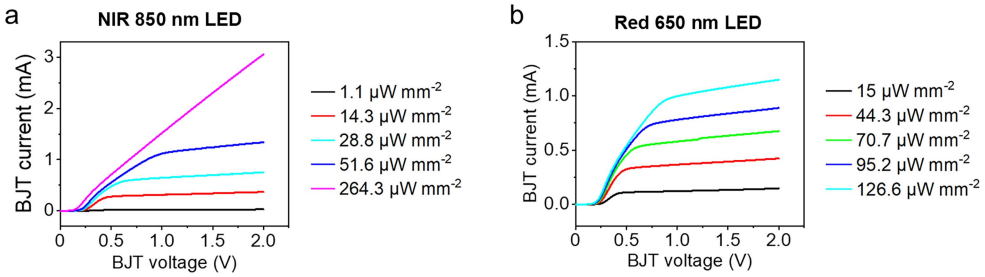

Extended Data Fig. 2 | Characteristics of bipolar junction transistor (BJT)-based phototransistors. a,**b**, Characteristic curves of the phototransistors under various light intensities emitted from a NIR LED (850 nm, **a**) and a red LED (650 nm, **b**).

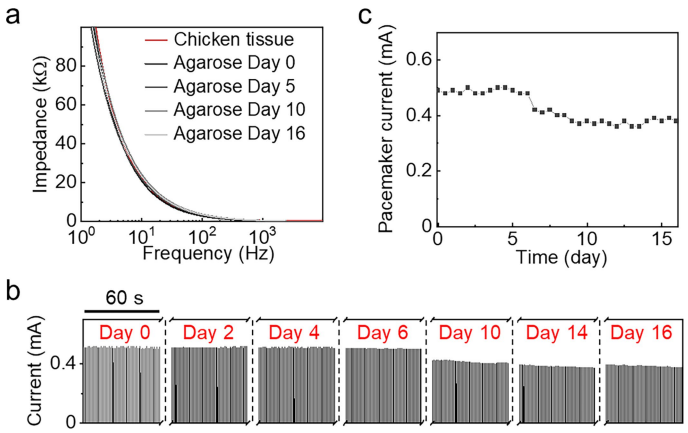

Extended Data Fig. 3 | Measurement of the operational lifespan of the device. a, EIS of an agarose gel and chicken tissue. **b**, The output currents of the pacemaker over days. **c**, Output currents of the pacemaker over days under pulsed illumination.

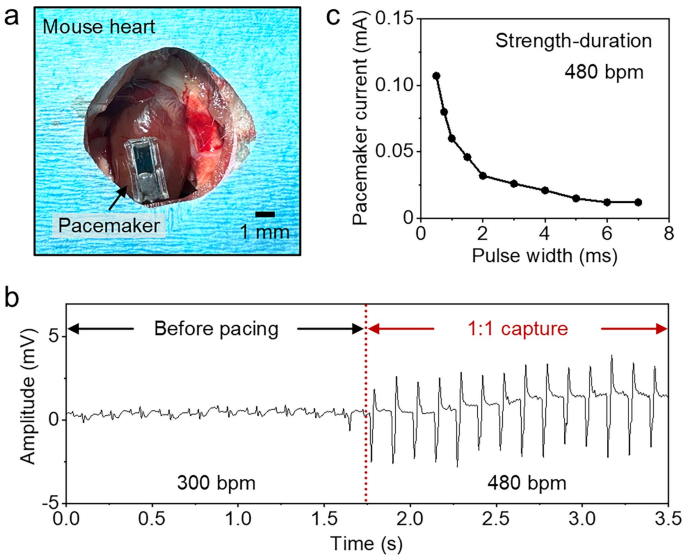

Extended Data Fig. 4 | In vivo demonstration of cardiac pacing in mouse models. a, Photograph showing a pacemaker placed on the surface of a mouse heart. **b**, ECG results before and during mouse heart pacing. **c**, Strength-duration curve when pacing at 480 bpm. n = 3 biologically independent animals.

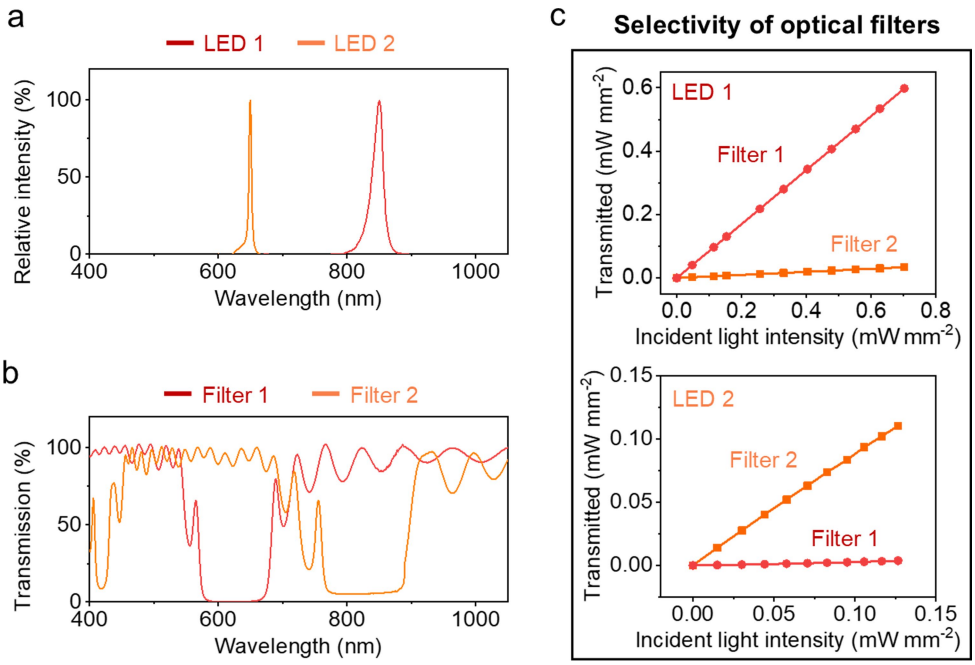

Extended Data Fig. 5 | Selection of LEDs and optical filters for multi-site, time-synchronized cardiac pacing. a, Emission spectra for LEDs 1 and 2. **b**, Transmission curves for filters 1 and 2. **c**, Transmitted light intensities as a function of incident intensities from LEDs 1 and (2) for filters 1 and 2.

nature portfolio

Corresponding author(s): John A. Rogers; Igor R. Efimov; Rishi K. Arora; Wei Ouyang; Yonggang Huang; Yamin Zhang

Last updated by author(s): Dec 14, 2024

Reporting Summary

Nature Portfolio wishes to improve the reproducibility of the work that we publish. This form provides structure for consistency and transparency in reporting. For further information on Nature Portfolio policies, see our Editorial Policies and the Editorial Policy Checklist.

Statistics

For all statistical analyses, confirm that the following items are present in the figure legend, table legend, main text, or Methods section.

n/a	Confirmed
☐	☒ The exact sample size (*n*) for each experimental group/condition, given as a discrete number and unit of measurement
☐	☒ A statement on whether measurements were taken from distinct samples or whether the same sample was measured repeatedly
☐	☒ The statistical test(s) used AND whether they are one- or two-sided *Only common tests should be described solely by name; describe more complex techniques in the Methods section.*
☒	☐ A description of all covariates tested
☒	☐ A description of any assumptions or corrections, such as tests of normality and adjustment for multiple comparisons
☐	☒ A full description of the statistical parameters including central tendency (e.g. means) or other basic estimates (e.g. regression coefficient) AND variation (e.g. standard deviation) or associated estimates of uncertainty (e.g. confidence intervals)
☐	☒ For null hypothesis testing, the test statistic (e.g. *F*, *t*, *r*) with confidence intervals, effect sizes, degrees of freedom and *P* value noted *Give P values as exact values whenever suitable.*
☒	☐ For Bayesian analysis, information on the choice of priors and Markov chain Monte Carlo settings
☒	☐ For hierarchical and complex designs, identification of the appropriate level for tests and full reporting of outcomes
☒	☐ Estimates of effect sizes (e.g. Cohen's *d*, Pearson's *r*), indicating how they were calculated

Our web collection on statistics for biologists contains articles on many of the points above.

Software and code

Policy information about availability of computer code

Data collection	The discharge behaviours were collected using a Landt battery tester. EIS relied on a Metrohm system. The characteristic responses of the PTs were collected using a PalmSens4 system. ECG was collected using PowerLab and Bio Amp (ADInstruments). Six-lead ECG was recorded using Prucka CardioLab. The Perkin Elmer LAMBDA 1050 spectrophotometer measured the transmission spectra of the filters. A Thorlabs' PM200 Optical Power and Energy Meter recorded the intensities of light from LEDs.
Data analysis	The following software were used in this study: PSTrace (v5.9), Prism (v10, GraphPad), OriginLab (v2019b), EC-Lab (V11.36), Labchart (v8) and MATLAB (R2023b). Custom Python code with Python 3.8.10 and Bleak 0.12.1, Scipy 1.7.3, Numpy 1.20.2, Pandas 1.2.5 and Matplotlib 3.3.4 was used to receive and analyse ECG data. The code for connecting to the device via BLE, recording and analyzing ECG data in real time, and configuring the pacing parameters in a closed-loop system is available on Code Ocean (https://codeocean.com/capsule/9406347/tree/v1).

For manuscripts utilizing custom algorithms or software that are central to the research but not yet described in published literature, software must be made available to editors and reviewers. We strongly encourage code deposition in a community repository (e.g. GitHub). See the Nature Portfolio guidelines for submitting code & software for further information.

Data

Policy information about availability of data

All manuscripts must include a data availability statement. This statement should provide the following information, where applicable:

- Accession codes, unique identifiers, or web links for publicly available datasets
- A description of any restrictions on data availability
- For clinical datasets or third party data, please ensure that the statement adheres to our policy

The main data supporting the results of this study are present in the paper and the Supplementary Information.

Research involving human participants, their data, or biological material

Policy information about studies with human participants or human data. See also policy information about sex, gender (identity/presentation), and sexual orientation and race, ethnicity and racism.

Reporting on sex and gender	N/ATissue received as declined for transplant was de-identified
Reporting on race, ethnicity, or other socially relevant groupings	Discarded and de-identified human tissue was provided by the Gift of Hope organ procurement organization (Chicago, IL). The Northwestern University Institutional Review Board (IRB) reviewed the submitted protocol of the study and determined that the proposed activity is not research involving human subjects.
Population characteristics	N/A
Recruitment	N/A
Ethics oversight	N/A

Note that full information on the approval of the study protocol must also be provided in the manuscript.

Field-specific reporting

Please select the one below that is the best fit for your research. If you are not sure, read the appropriate sections before making your selection.

☒ Life sciences ☐ Behavioural & social sciences ☐ Ecological, evolutionary & environmental sciences

For a reference copy of the document with all sections, see nature.com/documents/nr-reporting-summary-flat.pdf

Life sciences study design

All studies must disclose on these points even when the disclosure is negative.

Sample size	For in vivo pacing demonstrations, a number of n=3 mice and n=5 canines were utilized. Exceptionally, in closed-loop tests (Fig. 5), the authors used one rat and successfully proved the concept. For ex vivo pacing demonstrations, a number of n=3 pig hearts and n=5 human hearts were utilized. For in vivo biocompatibility tests, a number of n=3 rats were used. For in-vivo lifetime demonstration, a number of n=4 rats were utilized. The sample size for cardiac electrical stimulation was not predetermined but was instead based on laboratory experience. It was considered adequate to illustrate the representative effects of cardiac pacing with the pacemakers.
Data exclusions	No data points were excluded from analysis.
Replication	The devices performed similarly across multiple animal groups. ECG signals were recorded in multiple groups. The ex vivo cardiac pacing results represent data from more than three independent experiments conducted using different human and porcine hearts. The in vivo rat & mice heart pacing results reflect findings from over three independent experiments performed with various devices and animals. Similarly, the in vivo dog heart pacing experiment results are based on over three independent experiments using different devices and dogs.
Randomization	All animals were randomized into experimental groups. The ex vivo human heart pacing experiments were conducted on de-identified discarded tissues that did not involve human subjects prior to their procurement for research. No significant variability in response to cardiac pacing is anticipated.
Blinding	No blinding was attempted. We ensured that control and experimental groups were tested using the same experimental conditions whenever necessary, and that data from both groups were analyzed using the same criteria and methods.

Reporting for specific materials, systems and methods

We require information from authors about some types of materials, experimental systems and methods used in many studies. Here, indicate whether each material, system or method listed is relevant to your study. If you are not sure if a list item applies to your research, read the appropriate section before selecting a response.

Materials & experimental systems

n/a	Involved in the study
☒	☐ Antibodies
☐	☒ Eukaryotic cell lines
☒	☐ Palaeontology and archaeology
☐	☒ Animals and other organisms
☒	☐ Clinical data
☒	☐ Dual use research of concern
☒	☐ Plants

Methods

n/a	Involved in the study
☒	☐ ChIP-seq
☒	☐ Flow cytometry
☒	☐ MRI-based neuroimaging

Eukaryotic cell lines

Policy information about cell lines and Sex and Gender in Research

Cell line source(s)	L929 mouse fibroblast cells were provided by the Developmental Therapeutics Core at Northwestern University
Authentication	Cell lines were authenticated by the vendor.
Mycoplasma contamination	Cell lines were tested negative for mycoplasma contamination
Commonly misidentified lines (See ICLAC register)	No commonly misidentified lines were used

Animals and other research organisms

Policy information about studies involving animals; ARRIVE guidelines recommended for reporting animal research, and Sex and Gender in Research

Laboratory animals	In vivo rodent pacing study was performed on mice (15–25 weeks old; C57BL/6J; Jackson Laboratory; male and female) and rats (12-14 weeks old; Sprague–Dawley; Charles Rivers Laboratory; male). In vivo demonstration of pacemaker injection and cardiac pacing in large-animal models used retired breeder female and male hound dogs (age 1.6–4.5 years, weight 39-53 kg). In vivo biocompatibility tests used male rats (12-14 weeks old; Sprague–Dawley; Charles Rivers Laboratory; male). In vivo lifetime demonstration of pacemakers were performed on rats (12-14 weeks old; Sprague–Dawley; Charles Rivers Laboratory; male); All mice and rats were housed in the animal facility at Northwestern University, where the light/dark cycle was automatically controlled, with a maintained temperature range of 70–74°F and humidity levels between 30–70%. Porcine hearts were acquired from the Center of Comparative Medicine of Northwestern University as post-euthanasia tissue transfer.
Wild animals	The study didn't involve wild animals.
Reporting on sex	Both male and female rats and hound dogs were used in the cardiac pacing experiments. Male rats were used in the in vivo biocompatibility tests of control and device groups.
Field-collected samples	The study didn't involve samples collected from the field.
Ethics oversight	All experimental animal procedures and protocols were approved by Northwestern University Institutional Animal Care and Use Committee and in compliance with suggestions from the panel of Euthanasia of the American Veterinary Medical Association and the National Institutes of Health Guide for the Care and Use of Laboratory Animals.

Note that full information on the approval of the study protocol must also be provided in the manuscript.

Plants

Seed stocks	N/A
Novel plant genotypes	N/A
Authentication	N/A